Supplementary Information (SI) for Physical Chemistry Chemical Physics.
This journal is © the Owner Societies 2024

Electronic Supplementary Information

Ultrafast structural dynamics of UV photoexcited cis,cis-1,3-cyclooctadiene observed with time-resolved electron diffraction

Sri Bhavya Muvva[a,*], Yusong Liu[b,c], Pratip Chakraborty[d,e], Joao Pedro Figueira Nunes[a,†], Andrew R. Attar[b], Surjendu Bhattacharyya[f], Kurtis Borne[f], Elio G Champenois[b], Nathan Goff[g], Kareem Hegazy[b,h], Matthias C Hoffmann[b], Fuhao Ji[b], Ming-Fu Lin[b], Duan Luo[b], Lingyu Ma[g], Asami Odate[g], Shashank Pathak[f], Daniel Rolles[f], Artem Rudenko[f], Sajib Kumar Saha[a], Xiaozhe Shen[b], Xijie Wang[b,‡], Matthew R Ware[b], Stephen Weathersby[b], Peter M Weber[g], Kyle J Wilkin[a], Thomas J. A. Wolf[b], Yanwei Xiong[a], Xuan Xu[g], Jie Yang[b], Spiridoula Matsika[d], Thomas Weinacht[c], Martin Centurion[a,*]

[a.] *Department of Physics and Astronomy, University of Nebraska–Lincoln, Lincoln, Nebraska, USA. E-mail: bhavya.m@huskers.unl.edu ; martin.centurion@unl.edu*
[b.] *SLAC National Accelerator Laboratory, Menlo Park, California, USA.*
[c.] *Department of Physics and Astronomy, Stony Brook University, Stony Brook, New York, USA.*
[d.] *Department of Chemistry, Temple University, Philadelphia, Pennsylvania, USA.*
[e.] *School of Chemistry, Pharmacy and Pharmacology, University of East Anglia, Norwich NR4 7TJ, United Kingdom.*
[f.] *J.R. Macdonald Laboratory, Department of Physics, Kansas State University, Manhattan, Kansas, USA.*
[g.] *Department of Chemistry, Brown University, Providence, Rhode Island, USA.*
[h.] *Department of Physics, Stanford University, Stanford, USA.*
†Present address: Diamond Light Source Ltd, Didcot, UK.
‡Present addresses: Department of Physics, University of Duisburg-Essen 47052 Duisburg, Germany.; Department of Physics, University Dortmund, 44221 Dortmund, Germany.; Research Center Chemical Sciences and Sustainability, Research Alliance Ruhr, 44780 Bochum, Germany.

* Corresponding authors

This Document includes:

Supplementary Text

Table S1

Figures S1 to S20

Table of Contents

Section No.		Page No.
1.	Experiment data processing	3
2.	Trajectory surface hopping (TSH) simulations	3
3.	Static diffraction patterns signal calculation for simulated data	5
4.	Calculation of the difference diffraction signals from the simulations	6
5.	Calculation of static diffraction signals from experimental data	7
6.	Detector pixel calibration	7
7.	Determination of experiment difference signals - ΔsM(s,t), and ΔPDF(r,t)	7
8.	Comparison of experiment and simulated difference diffraction signals	9
9.	Determination of excitation fraction	10
10.	Pump power selection	10
11.	Dynamics due to changes in the carbon distances after excitation	10
12.	Ring motion after excitation	11
13.	Oscillations in ΔPDF signal for all end-products	12
14.	Comparison of reaction coordinates	12
15.	Fitting Analysis	14
16.	Supplementary Table	16
17.	Supplementary Figures	17
18.	Supplementary References	37

1. Experiment data processing

We processed all the images containing diffraction patterns using the following sequence of steps to extract the 1-D scattering intensity signal in momentum space for all the delay points, $(I_{\mathrm{exp}}(s,t))_{1-4}$:

1) The background signal was calculated from the images collected without the electron beam, and this background signal was subtracted from each diffraction image.
2) Ellipticity correction was performed on all images by taking solid data diffraction pattern as reference.
3) To remove the detector baseline, the mean value of the four corners outside the phosphor screen from the image was subtracted from the total image.
4) For every image, the mean intensity of pixels with same detector coordinates at the same time delay was calculated, and the pixels having an intensity exceeding four times the standard deviation over the mean were eliminated.
5) The image was masked over the center region to remove contributions from the hole in the detector, and other detector artifacts. The hole in detector is for un-diffracted electrons to pass through it.
6) A common center for all images was determined by taking the average of center positions of the static diffraction pattern images, as the delay-dependent shift in center values was below 1 pixel.
7) In each image, the mean intensity of pixels which are located at the identical radial distance was calculated, and pixels having an intensity exceeding three standard deviations above the mean were removed. Finally, a median filter with a 5×5 kernel size was applied on all images to remove noise.
8) After performing the above data cleaning steps, the final center for each image was calculated. The average center of the static diffraction pattern images was used as the center for all the images.
9) The 1 D averaged signal at each radius is calculated and then this 1 D signal is normalized using the mean counts between 3.2 and 6.1 $Å^{-1}$ to get the 1-D scattering intensity signal in momentum space, $I_{\mathrm{exp}}(s,t)$.

2. Trajectory surface hopping (TSH) simulations

We performed trajectory surface hopping (TSH) simulations at the extended multi-state complete active space second order perturbation theory (XMS-CASPT2) level[5–7]. Since both conformers of cis,cis-1,3-cyclooctadiene (cc-COD) showed similar dynamics and similar time scales at the CASSCF level[8], TSH at the XMS-CASPT2 level was performed for only the lowest energy conformer of cc-COD[9]. We used the same 200 initial conditions (ICs) sampled from the ground-state Wigner distribution of a harmonic oscillator at 298 K (used in the CASSCF[10] TSH calculations[8]). For on-the-fly electronic structure calculations, three-state averaging with an active space of 4 electrons in 4 orbitals (SA3-CAS(4,4)) was employed with cc-pVDZ[11] basis set (together with its corresponding density-fitted basis set (cc-pVDZ-jkfit)) at the XMS-CASPT2 level since such a setup provided the best compromise between accuracy (state ordering at the FC

region) and computational cost (on-the-fly trajectory propagation). In addition, the XMS-CASPT2 calculations used the single-state single-reference (SSSR) contraction scheme and an imaginary shift (to remove intruder states) of 0.2 au. The dynamics were propagated from the bright S_1 state for all ICs using Newton-X[12,13]. On-the-fly energies, gradients, and nonadiabatic couplings were generated using the Bagel package[14,15]. The fewest switches surface hopping (FSSH)[16] algorithm was employed to take into account non-adiabatic coupling (NAC) amongst the S_2, S_1, and S_0 states. Decoherence corrections were taken into account using the approach of non-linear decay of mixing by Granucci and Persico[17] with the recommended value of the empirical parameter, $\alpha = 0.1$ Hartree[18]. The velocity Verlet algorithm was used to integrate Newton's equations of motion with a time step of 0.5 fs. The semiclassical time-dependent Schrödinger equation was integrated using fifth-order Butcher's algorithm with a time step of 0.005 fs. After the hops, the kinetic energy was corrected by adjusting momentum along the direction of the nonadiabatic coupling vector. Additionally, after the frustrated hops, the momentum direction was left unaltered. The simulations were performed for 400 fs using XSEDE's computational resources[19].

Some of the trajectories failed before reaching 400 fs. We discarded about 64 out of a total of 200 trajectories that failed within 200 fs due to failure of energy conservation. Some of these failed very quickly (within 30 fs) without any hop, others failed on S_1 and S_2 states and soon after $S_1 \rightarrow S_0$ hop. Another 20 trajectories were also discarded due to various reasons including: energy fluctuations, active space deterioration. As it's not feasible to definitively determine the outcomes of these failed trajectories, we excluded them from the population count.

The remaining 116 trajectories were sorted into groups by their end products, and the percentage of each products formed is estimated. As discussed in the main paper, these trajectories form seven types of end-products, including – hot cc-COD, cis,trans-1,3-cyclooctadiene (ct-COD) and bicyclo [4.2.0] oct-7-ene (BCO) , and four other end-products which behave either like cc-COD or ct-COD in which hydrogen migration takes place across the ring between C5 to C1 and C8 to C4 : ([1,5]-H-shift-cc-COD, [4,8]-H-shift-cc-COD, [1,5]-H-shift-ct-COD and [4,8]-H-shift-ct-COD). The structures of these end-products are shown in Figure S1. The photoproducts with both the H-C=C-H dihedral angles close to zero degrees (0°) are classified as hot cc-COD products, and ct-COD refers to the photoisomer product where one of the H-C=C-H dihedral angles in the molecule is close to 180 degrees (180°). BCO is an electrocyclic ring-closed product with two rings. A separate theoretical study also predicted similar products as those identified in our calculations[20].

The products with hydrogen migration behaving like cc-COD or ct-COD are structurally similar to cc-COD or ct-COD (this is further discussed and shown in section: 'Fitting analysis'), and so, we can't distinguish these products experimentally with UED measurements. Thus, we classified the end-products into 3 categories based on the structure: hot cc-COD, ct-COD and BCO. The number and percentage of trajectories forming each end-product is shown in Table 1. The end-products yields from the trajectory simulations are 63% hot cc-COD, 32% ct-COD and 5% BCO. From the trajectories forming BCO end-products, it is observed that the trajectory first forms ct-COD in ground state (S_0), which then gets converts to BCO.

Out of the 116 trajectories forming products in ground state (S_0 state), only 89 trajectories completely ran till 400 fs without failing. To compare the total simulated signal with the experiment signal, we calculated the average of the diffraction signal from the 95 selected

trajectories that lasts longer than delays 350 fs (~ 47.5% of the total). We chose this delay value to ensure each end-product has a possible sufficient number of trajectories.

We found most of the trajectories have multiple hops and back hops within S_1 and S_0 states before the final hop from S_1 to S_0 state, which is taken to be the hopping time of that trajectory. The hopping times of the selected trajectories are all found to be less than 250 fs as shown in main paper Figure 5 and 6. Refer to Figure S2 showing the population decay from the excited to the grounded state as a function of time.

Figure S3 shows the calculated absorption cross-section spectrum of cc-COD for deep UV wavelengths range as shown in Liu et al.[9].

3. Static diffraction patterns signal calculation for simulated data

We simulated 1D diffraction signals of all the molecular geometries of the TSH dynamics simulated trajectories to compare with experimental data. The diffraction signals were calculated using the independent atom model (IAM). The total diffraction signal in momentum space ($I(s)$) for a molecular geometry can be expressed as the sum of the atomic scattering intensity I_{at} and the molecular scattering intensity I_{mol}, as below:

$$I(s) = I_{mol}(s) + I_{at}(s) \tag{S1}$$

Here, s is the momentum space vector and is defined as:

$$s = \frac{4\pi}{\lambda}\sin\left(\frac{\theta}{2}\right) \tag{S2}$$

Where, λ is the incident electrons wavelength and θ is the angle between the incident and scattered electrons.

The atomic scattering term $I_{at}(s)$ is the scattering intensity from each atom in the molecule and does not contain structural information. It is defined as:

$$I_{at}(s) = \sum_{i=1}^{N} f_i^*(s) f_i(s) \tag{S3}$$

In Eq. (S3), $f_i(s)$ is the scattering amplitude (form factor) of the i^{th} atom, this is calculated using the ELSEPA program[21] for 3.7 MeV incident electrons.

The molecular scattering term ($I_{mol}(s)$) comprises of the structural information of the molecule. It contains information of the internuclear distances between every pair of atoms within the molecule, and is expressed as shown below:

$$I_{mol}(s) = \sum_{i=1}^{N}\sum_{j=1, j\neq i}^{N} f_i^* f_j(s)\frac{\sin\left(sr_{ij}\right)}{sr_{ij}} \tag{S4}$$

Where N is number of atoms in the molecule, r_{ij} is the distance between the i^{th} and the j^{th} atom.

The diffraction signal is typically presented in the form of modified scattering intensity (sM(s)), which is defined as:

$$sM(s) = \frac{I_{mol}(s)}{I_{at}(s)}s \tag{S5}$$

sM(s) serves to enhance the oscillations in the I_{mol} term and suppress the drop in scattering intensity terms by the increase in s.

The sinusoidal transformation of sM(s) term from momentum transfer space into real space yields an atomic pair distribution function (PDF), it is calculated as shown below:

$$PDF(r) = \int_0^{s_{max}} sM(s) \sin(sr) e^{-ks^2} ds \tag{S6}$$

Here, r represents the interatomic distances, s_{max} is the maximum detectable diffraction pattern in momentum space, which is limited by the detector screen size, and this is set as 12 $Å^{-1}$ in the simulations, and k is the damping factor which is set to 0.03 (k = 0.03) to minimize artifacts due to the finite limit of data and edge effects. The PDF contains information of all contributing interatomic distances in the molecule[1–4].

4. Calculation of the difference diffraction signals from the simulations

We calculated the difference diffraction signals in momentum space ($\Delta sM(s,t)$) at each delay point for the trajectories simulated, by subtracting $sM(s,t)$ with the average static modified intensity ($sM^{static}(s)$). We calculated $sM^{static}(s)$ by taking average of $sM(s,t=0)$ at t=0 from all trajectories. We next obtained static pair distribution function $PDF^{static}(r)$ by taking sine transform of $sM^{static}(s)$ using Eq. (S6).

$$\Delta sM(s,t) = sM(s,t) - sM^{static}(s) \tag{S7}$$

This is equivalent to

$$\Delta sM(s,t) = s\frac{I_{mol}(s,t) - I_{mol}(s,t=0)}{I_{at}(s)} \tag{S8}$$

We further obtained the difference diffraction signal in real space ($\Delta PDF(r,t)$) (difference pair distribution function) at each delay point by taking the sine transform of $\Delta sM(s,t)$ as below:

$$\Delta PDF(r,t) = \int_0^{s_{max}} \Delta sM(s,t) \sin(sr) e^{-ks^2} ds \tag{S9}$$

For comparing the simulated difference diffraction signals data with the experiment data, we applied a convolution with a Gaussian function with 150 fs full width at half maximum (FWHM) in time to the simulated signals of $\Delta sM(s,t)$ and $\Delta PDF(r,t)$, to match the experimental instrument response function.

5. Calculation of static diffraction signals from experimental data

The experimental static modified scattering intensity, ${}^{sM}{}_{exp}^{static}(s)$ is calculated using the method developed by Ihee et al[22], as it cannot be calculated using Eq. (S5), since $I_{mol}(s)$ and $I_{at}(s)$ cannot be separated in experiment. ${}^{sM}{}_{exp}^{static}(s)$ is expressed as:

$$sM_{exp}^{static}(s) = \frac{I_{\exp}(s,t<0) - I_{bkg}}{I_{at}(s)} s \tag{S10}$$

Here ${}^{I}{}_{\exp}(s,t<0)$ is the reference experimental scattering intensity signal, which corresponds to static unpumped diffraction signal. This signal is obtained by averaging the 1-D diffraction signal measured at delays -800 fs < t < -100 fs. $I_{bkg}(s)$ is the experimental background signal which consists of signal from atomic scattering signal and background from the instrument. $I_{bkg}(s)$ is calculated by fitting a sum of exponents through s values which correspond to the zero-crossing of the simulated static molecular scattering term $(I_{mol}(s,t=0))^2$. Here, ${}^{I}{}_{at}(s)$ is the atomic scattering intensity obtained from theoretical calculation (Eq. (S3)).

The experimental static ${}^{PDF}{}_{exp}^{static}(r)$ is calculated by sine transformation of the ${}^{sM}{}_{exp}^{static}(s)$ using Eq. (S6). We compared the static PDF for both experiment and simulation in Figure 2a of the main paper. The theory simulated signal was scaled by a factor of 0.5 to match the experimental signal.

6. Detector pixel calibration

The calibration of the detector pixel size to the momentum transfer vector, s, was performed using a reference Bi_2Te_3 solid sample at the start of experiment. The known positions of Bragg reflection from a Bi_2Te_3 crystal sample were used for this calibration. The value of this conversion was further optimized by comparing the theoretical (Eq. (S3)) and experimental static (${}^{sM}{}_{exp}^{static}(s)$) scattering signals for COD. This calibrated value (1 pixel = 0.0247 $Å^{-1}$) was used for all the analysis.

7. Determination of experiment difference signals - ΔsM(s,t), and ΔPDF(r,t)

The details of the diffraction signals calculation from experiment data are described in detail elsewhere [1–4]. The time-dependent difference scattering intensity for experiment data, ${}^{\Delta I}\!/_{I}{}_{exp}(s,t)$, is calculated as:

$$\frac{\Delta I}{I}_{exp}(s,t) = \frac{I_{\exp}(s,t) - I_{\exp}(s,t<0)}{I_{\exp}(s,t<0)} \quad \text{(S11)}$$

Here, $I_{\exp}(s,t)$ is the 1-D scattering intensity experimental data at each delay point.

The time-dependent difference-modified scattering intensity for experimental data, $\Delta sM_{exp}(s,t)$, is calculated as:

$$\Delta sM_{exp}(s,t) = \frac{I_{\exp}(s,t) - I_{\exp}(s,t<0)}{I_{at}(s)} s \quad \text{(S12)}$$

We observed systematic offsets at high s in the experimental ΔsM signal, due to the unaccounted background by the difference-diffraction method. At each delay point, a power fit ($a*sb+c$) is fitted to $\Delta sM_{exp}(s,t)$ and subtracted from it, to account for this offset at high s[23,24]. This is followed by subtraction of a 2nd order polynomial from the signal to account for the offsets at low s, as the power fit does not have much effect on data at low s. These fits in s assumes the signal is oscillating with respect to a zero baseline. However, this method may not completely remove all the offset effects that could be present in the data, leading to the discrepancy observed between experimental and simulated data. Figure S4 shows the $\Delta sM_{exp}(s,t)$ without and with these fits applied.

We performed the bootstrap analysis, using the method explained below, to compute 200 datasets of $\Delta sM_{exp}(s,t)$ for all delay points. We then removed the systematic offsets observed in all these datasets using the procedure above. Fig. S4 shows the error bars in $\Delta sM_{exp}(s,t)$, which represent uncertainties within one standard deviation of the measurements, across the bootstrapped datasets.

Error estimation in experiment data by bootstrap analysis:
A standard bootstrapping analysis was employed to estimate the statistical uncertainty of the experimental signal. At each pump-probe delay, we recorded 'n' images, where n is equal to 273. Let's refer to the n images as a dataset. We calculated the 1-D difference-modified scattering intensity signals dataset in momentum space for each dataset. For each delay, we randomly selected n images from the dataset with replacement to create a new dataset. We repeated this 200 times to generate 200 new datasets at each delay. This method generates 200 datasets of 1-D modified scattering signals in momentum space for all delay points. We independently analyzed each bootstrapped dataset to obtain the diffraction signals in real space. The mean of the dataset provides the signal at each delay, which we used as the experimental results in the manuscript. One standard deviation of all the datasets gives the uncertainty of the experiment measurements.

Final experiment difference diffraction signal in momentum space:
The final experimental $\Delta sM(s,t)$ at each delay point is calculated by taking average of 200 bootstrapped datasets and applying smoothing of data in momentum space (using moving average of s = 0.17 $Å^{-1}$). One-standard deviation across these bootstrapped datasets is computed to estimate the uncertainty errors of the measurements.

Final experiment difference diffraction signal in real space:
Similarly, the final experimental $\Delta PDF(r,t)$ is calculated by taking an average of 200 bootstrapped datasets of difference diffraction signal in real space $(\Delta PDF_{exp}(r,t))$, and we computed the one-

standard deviation across these bootstrapped datasets to determine the errors in experimental data. We computed $^{\Delta PDF_{exp}(r,t)}$ for all the bootstrapped datasets by following the below procedure.

$\Delta PDF_{exp}(r,t)$ at each delay point is calculated by taking the sine transform of $\Delta sM_{exp}(s,t)$ from 0 to the maximum detectable diffraction pattern value in momentum-space. However, we don't have experiment data for values of s < 0.6 $Å^{-1}$ due to the hole in detector for un-diffracted electron beams. To avoid artifacts in calculation of $^{\Delta PDF_{exp}(r,t)}$, the missing low-angle data ($^{\Delta sM_{exp}(s<0.6,t)}$) was linearly extrapolated to $s = 0$, to get $^{\Delta sM'_{exp}(s,t)}$. We applied smoothing to $^{\Delta sM'_{exp}(s,t)}$ in momentum space, using a moving average of s = 0.17 $Å^{-1}$. This modified $^{\Delta sM'_{exp}(s,t)}$ was then used to calculate the time-dependent difference pair distribution functions, $^{\Delta PDF_{exp}(r,t)}$, as:

$$\Delta PDF_{exp}(r,t) = \int_0^{s_{max}} \Delta sM'_{exp}(s,t)\ \sin(sr) e^{-ks^2} ds \tag{S13}$$

The damping factor, k was set to 0.035 and s_{max} is 12 $Å^{-1}$.

Time zero determination in experiment's signal:

We initially estimated time zero ($T'_0 = 0\ fs$) of pump and probe pulse, by using a solid sample at the start of the experiment. The initiation of the heating signal from the sample was taken as T'_0. The absolute time zero (T_0') of the experimental total data is corrected by a quantitative comparison with simulations. Figure S5 shows the experimental and simulated $\Delta PDF(r,t)$ integrated in the region 2.6 < r (Å) < 3 (defined as β region in main paper) for both experiment and simulated signal. The experimental signal in the figure has smoothing applied in time (gaussian of 100 fs FWHM), and the simulation data is convolved with the instrument response function (IRF) of 150 fs FWHM in gaussian. The experiment data with respect to time delays determined by solid sample ($Delay_{solid}$) appears to be shifted by 300 fs compared to simulated signal. To align the experiment and simulated data time scales, all the experiment data's delay points were shifted by 300 fs with respect to $Delay_{solid}$. After applying the delay shift, the new time zero of the experiment data is set to $T_0 = 0$ fs, where $T_0 = T_0'$ - 300 fs. These adjusted delay points were used for all the time dependent analysis presented in the main paper and following sections. We also note here that this shift in delay is close to the experimentally determined time zero, $t'_0 = 266\ fs$, from the error function fit described below.

We calculated the integrated intensity signal ($\Delta PD(t)$) by taking the summation of the absolute value of the mean of $^{\Delta sM_{exp}(s,t)}$ within the following regions: 2.1 < s ($Å^{-1}$) < 2.85, 3.4 < s ($Å^{-1}$)< 4 and 5.9 < s ($Å^{-1}$) < 6.5. We used an error function fit ($F(t)$) to determine the onset of this integrated intensity signal ($\Delta PD(t)$)[4].

$$F(t) = a + b * erf\left(2.\sqrt{\ln(2)}\,\frac{t - t_0}{\tau}\right) \tag{S14}$$

Where, a is a constant offset, b the signal amplitude, t_0 is the error function's center and τ is the width of the error function. We found the center of the error function fit to be $t'_0 = 266\,fs$, this determines the onset time (time-zero) of the signal from the experiment data.

8. Comparison of experiment and simulated difference diffraction signals

Figure S6 shows the comparison between experimental and simulated static $sM(s)$ and $\Delta sM(s,t)$. There is a good agreement between experimental results and simulated signal from theory. The experimental and simulated difference diffraction signals in real space ($\Delta PDF(r,t)$) are shown in Figure 3 of the paper. The experimental data in these figures and the main paper is smoothed in time by Gaussian convolution of 100 fs FWHM. The simulated data in these figures is convolved with a Gaussian function of 150 fs FWHM to match the experimental instrument response function (IRF)[25,26].

Figure S6 (d) shows the comparison of experimental and simulated signals in momentum space, both the signals are averaged for delays between 250 fs to 400 fs. There is a good agreement between experiment results and simulated signal from theory. We can observe some differences between the experimental and simulated signals, the experimental signal seems to follow a similar pattern as the theory signal with the position of peaks and valleys mostly matching, but the experiment signal has a baseline shift. This baseline shift is likely caused by the power and polynomial fits which is applied to experimental data to remove the offsets from the signal (described above in section 7). The fits forces experiment signal to oscillate with respect to zero, and this leads to the discrepancy observed between experimental and simulated data. This artifact observed in experimental $\Delta sM(s,t)$ gets transferred to the calculation of experimental $\Delta PDF(r,t)$ and accounts for a significant part of the difference observed between the experimental and theoretical $\Delta PDF(r,t)$ as observed in main text in Figure 2b.

9. Determination of excitation fraction

We estimated the experimental excitation percentage by comparing experimental ($\Delta sM_{exp}^{avg}(s)$) and simulated ($\Delta sM_{sim}^{avg}(s)$) diffraction signals averaged between 250 fs and 400 fs. A scaling factor (scale) was multiplied with $\Delta sM_{sim}^{avg}(s)$, and a reduced chi-square fit (χ^2) was calculated for the $\Delta sM_{exp}^{avg}(s)$ and scale$*\Delta sM_{sim}^{avg}(s)$ over the region between 1.25 Å^{-1} and 7.5 Å^{-1}, By varying the scaling factor[1,2].

χ^2 value between the experimental and simulated diffraction signal:

$$\chi^2 = \sum_{s\,(\text{Å}^{-1}) = 2.55}^{7.5} \left(\frac{\Delta sM_{sim}^{avg}(s) - scale * \Delta sM_{sim}^{avg}(s)}{\sigma_{exp}(s,t)} \right)^2 \tag{S15}$$

where $\sigma_{\text{exp}}(s,t)$ is the experimental uncertainty value for the $\Delta sM_{exp}^{avg}(s)$ signal. The minimum of χ^2, which determines the best fit between experiment and simulation signal, was found at scale = 0.0325. Thus, the excitation percentage was determined to be 3.25%.

10. Pump power selection

We measured the difference diffraction patterns at five different pump pulse intensities (between 5 μJ to 30 μJ) and computed the integrated absolute intensity values in different regions of momentum space corresponding to these pump energies. For our time-dependent experiments, we selected the pump pulse energy of 15 μJ which was in the linear regime, to ensure single-photon excitation.

11. Dynamics due to changes in the carbon distances after excitation

The simulated structure of ground state cc-COD molecule (averaged over all trajectories) is shown in the main text in Figure 1 in different viewing planes, highlighting the flexibility of the molecule's ring. The distribution of R_{2C}, R_{3C}, R_{4C} and R_{5C} carbon distances in the ground state of all trajectories, which represents the distance between three, four and five consecutive carbon atoms in the ring, respectively, is shown in Figure 2. Excitation of the cc-COD molecule to the S_1 state triggers a ring motion which changes these carbon distances leading to the increase and depletion of ΔPDF signal across various regions with time delay. The three main positive signals in the time-dependent ΔPDF signal appear in regions α ($1.6 < r(\text{Å}) < 2.3$), β ($2.6 < r(\text{Å}) < 3$), and γ ($3.6 < r(\text{Å}) < 4.3$), as seen in Figure 3 of the paper.

Figure S7 depicts the changes in R_{2C}, R_{3C}, R_{4C} and R_{5C} distances over different time delays for all trajectories simulated. At delay=0, R_{2C} distances are concentrated around 1.5 Å region. Following excitation, we see a depletion in this region as these distances spread to the α region. Similarly, R_{3C} distances which are initially located around 2.4 Å, spread to both the α and β regions after excitation causing depletion around 2.4 Å. In the ground state, we can observe that R_{4C} and R_{5C} distances are split into 2 groups in regions between 3 Å to 4 Å, this is clearly seen from the double gaussian distribution of $R_{4C}\ and\ R_{5C}$ distances in Figure 2 of the main paper. Let's call earlier ones as shorter distances and the later ones as longer distances, which are in perpendicular direction to the shorter distances. Upon excitation there is a depletion in the region around 3.4 Å due to the spreading of shorter R_{4C} and R_{5C} distances to β region, and simultaneously spreading of longer R_{4C} and R_{5C} distances to γ region. We can also observe that certain R_{4C} distances spreads to the α region, these distances correspond to the new bond formed in the BCO trajectories, which results in the strong positive feature in ΔPDF signal in α region in these trajectories (refer to Figure S10). These changes in the distances contribute to the features observed in the time-dependent ΔPDF signal.

From Figure 5 of the main text, we can see the longest R_{5C} and shortest R_{5C} distances in the ring increase after excitation up to 20 fs, for all trajectories. After this delay, the longest R_{5C} continues to increase to reach a maximum (in γ region) around 70 fs and simultaneously, shortest R_{5C} decreases to reach a minimum (in β region). This behavior is coherent with respect to all the R_{5C} distances from all trajectories, and a similar behavior is followed by the R_{4C} distances. From Figure S8, we can clearly that the shortest $R_{4C}\ and\ R_{5C}$ distances along with the longest R_{3C} distances are collectively concentrated in β region for delays < 100 fs, after which this behavior is lost. Thus, these distances together cause intensity modulation observed in the β region. During this time, the longest $R_{4C}\ and\ R_{5C}$ distances are not concentrated at the same place in γ region, so there is no

intensity modulation in this region. In Figure S8 we can clearly see that as the longest R_{4C} distances stretch to γ region, the longest R_{5C} distances stretch further away.

12. Ring distortion motion after excitation

We can see in Figure S7, all the carbon distances of all trajectories initially increase for the first 20 fs after excitation. This indicates that the molecule's ring undergoes expansion initially. The spread of unbonded carbon atoms distances to both shorter and longer distances from a region indicate that the ring is stretching in a direction, and simultaneously compressing along the perpendicular direction. This motion is termed as ring distortion motion in the main paper.

This ring distortion motion is clearly tracked by the difference of maximum and minimum R_{5C} distances with delay as shown in Figure 5 and Figure 6 of the paper. From Figure 6, we observe that this motion is coherent for delays till 70 fs with respect to all trajectories, and at longer delays this coherent motion is absent. This behavior is seen from the lower spread of the error bars around the mean ring stretching parameter till around 70 fs. From the hop-times distribution, we found that 74 fs is the most likely time taken for the wavepacket to reach the Conical Intersection (CI) seam. The coherence behavior across the trajectories indicates that after the initial expansion, the ring starts to stretch in a direction and simultaneously compress in the perpendicular direction until the wavepacket reaches the CI seam. After this point, the wavepacket spreads quickly as the molecule reaches the ground state and multiple products are formed, this behavior is evident from the loss of coherence across the distances after CI seam. Thus, the ring distortion motion parameter is a good reaction coordinate describing the observed dynamics after photoexcitation of cc-COD molecules.

The ring stretches in a manner such that the separation (distance) between double bonds in the molecule decrease till reaching the CI seam, following an initial increase in the double bond distances when the ring expands. Refer to Figure S9 showing the behavior of change in double bonds distances as the ring stretches.

13. Oscillations in ΔPDF signal for all end-products

The signal corresponding to the end-product is calculated by taking the average of the combined signal from trajectories. The end-products classification is described in the main paper and SI section 2. The ΔPDF signal corresponding to each end-product is shown in Figure S10, distinct features in the signals are observed across the regions in real space.

We can see that all products have intensity modulations in the β ($2.6 < r(\text{Å}) < 3.0$) region. This behavior is due to the collective appearance of R_{3C}, R_{4C} and R_{5C} distances in this region after excitation for delays<100 as discussed in SI section 11. The ΔPDF signal average in the β region is shown in Figure S11 on the left y axis, and the ring stretch parameter is shown on the right y axis for each product. There is a clear correlation between the ring distortion motion parameter and the ΔPDF signal average in the β region in each product.

Figure 6 in the main text shows the same behavior due to the ring motion, for both simulated and experiment data. By comparison with the end-product signals separately, we can identify that the motion in the hot cis-cis product is similar to the motion in the total signal (in Figure 6). This indicates that the oscillations past 400 fs observed in the experiment mostly comes from the ring motion in the trajectories forming the hot cc-COD product. We can further interpret that in the trajectories forming ct-COD and BCO products, which requires large structural changes, the energy in this ring oscillation mode quickly spreads to other vibrational modes in the ground state.

14. Comparison of reaction coordinates

In this section, we compare the ring distortion parameter reaction coordinate with that of bond length alternation (BLA), torsional, and pyramidalization. The bond length alternation (BLA) motion can be used as a measure of double bonds stretching. We found all these motions are taking place after photoexcitation of cc-COD with 200 nm to S_1 state but none of the other motions oscillate on the same time scale as the ring distortion, and they undergo multiple oscillation periods before the molecule reaches the CI. The ring distortion, on the other hand, changes monotonically between excitation and reaching the CI, which makes it preferable as a reaction coordinate.

From our below comparisons, we conclude that all these motions of BLA (double bond stretching), torsional angles twisting, changing of pyramidalization angles are taking place after photoexcitation of cc-COD with 200 nm to S_1 state but they are not strongly correlated with the ring distortion motion.

Bond length alternation motion:
We observed that the BLA motion plays a significant role in these dynamics after photoexcitation (Figure S12), this was also reported in reference[8]. BLA coordinate is defined as

$$BLA = R_{C_1=C_2} - R_{C_2-C_3} + R_{C_3=C_4} \qquad (S16)$$

The $R_{C_1=C_2}$, $R_{C_2-C_3}$, $R_{C_3=C_4}$ are labelled in the Figure S12. We can see the coherence motion across the trajectories up to CI seam (t = 74 fs) in the BLA coordinate, during which there is large amplitude oscillation in mean BLA coordinate with a period of approximately 25 fs. After the CI, the mean BLA oscillation amplitude decreases significantly and shows a loss of coherence across trajectories. Figure S13 shows the comparison of the evolution of BLA coordinate with the ring distortion coordinate. We can see that both coordinates of ε and BLA are signatures of the CI, as there is coherence motion across the trajectories over the time the wavepacket takes to reach the CI seam, after which this behavior is lost.
There is no direct correlation between the ring stretching and the BLA, since they clearly oscillate with different frequencies. The linear correlation between the parameters can be quantified with the Pearson correlation coefficient (PCC), with PCC value of +1 indicating perfectly correlated and -1 indicating complete anti-correlation between the features. The PCC value between ε and BLA for delays up to 74 fs is equal to -0.1.

Torsional angle reaction coordinate:
Figure S14 shows the cc-COD ground state molecule with labelling of Carbon and hydrogen atoms.
Let's refer to the torsional angles of the two double bonds as Torsional angle 1 and Torsional angle 2. Torsional angle 1 is the dihedral angle around the C4=C3 bond, i.e. the angle H12-C4=C3-H11, and the Torsional angle 2 is the dihedral angle around the C2=C1 bond, i.e. the angle H10-C2=C1-H9. These torsional angles definitions are consistent with those in *Chakraborty et al.*[8] and are referred to as twist angles in *Chakraborty et al.*[8].

From Fig. S15 (a), we can see that the mean value of Torsional angle 1 decreases for the first 30 fs and then slowly recovers. Torsional angle 2 shown in Fig. S15 (b) shows no significant motion. There is no coherence motion across the trajectories up to CI seam. These tortional do not seem to be correlated with the ring distortion. The PCC value between ε and Torsional angle 1 is -0.47 and the PCC value between ε and Torsional angle 2 is 0.79.

Pyramidalization angle reaction coordinate:
Let's refer to the inner pyramidalization angles of the two double bonds as inner pyramidalization 1 and inner pyramidalization 2, and outer pyramidalization angles of the two double bonds as outer pyramidalization 1 and outer pyramidalization 2. The definitions of angles are consistent with the definitions in *Chakraborty et al.*[8].
Inner pyramidalization 1 is the dihedral angle C4=C3-H11-C2, and the inner pyramidalization 2 is the dihedral angle C3-C2-H10-C1. Outer pyramidalization 1 is the dihedral angle C5-C4-H12-C3, and the outer pyramidalization 2 is the dihedral angle C2=C1-H9-C8. Refer to the Figure S14 for the cc-COD ground state molecule, with Carbon and hydrogen atoms labeled.
From Fig. S16 (a), we can see that the inner pyramidalization angle 1 has coherence motion across the trajectories up to around 50 fs, and the inner pyramidalization angle 2 shown in Fig. S16 (b) shows no coherence motion. A similar behavior is seen for the outer pyramidalization angle 1 and outer pyramidalization angle 2 in Fig. S17. The outer pyramidalization angle 1 in Fig. S17 (a) has coherence motion across the trajectories up to around 50 fs, and after this duration, this behavior is lost and outer pyramidalization angle 2 in Fig. S17 (b) has no coherence motion across the trajectories.
Again, here there is no clear correlation between these coordinates and the ring distortion. The PCC value between ε and inner pyramidalization angle 1 is -0.7, but this angle is oscillating with a significantly faster period compared to the ring distortion. The PCC value between ε and the inner pyramidalization angle 2 is -0.17, the PCC value between ε and the outer pyramidalization angle 1 is 0.22, and PCC value between ε and outer pyramidalization angle 2 is 0.58.

15. Fitting analysis

The molecule returns to ground state before 250 fs, so the signal above 250 fs corresponds to the structures in the ground state. The signal of each end-product is calculated by taking the average of the simulated ΔsM for delays 250 fs <t < 400 fs. We used the averaged ΔsM signals from the combined hot cc-COD, combined ct-COD and BCO (shown in Figure S18) as the basis to fit both

the total simulated signal and experimental signal averaged for delays between 250 fs to 400 fs with a reduced chi-square function ($^{Ft(c,\,t_j)}$):

$$Ft(c,\,t_j) = \sum_{s}\sum_{i\,=\,1}^{n} \frac{1}{\sigma(s,t_j)^2} * \left[c_i(t_j) * \Delta sM\,{}_{i}^{basis}(s) \;-\; \Delta sM\,(s,t_j)\right]^2 \tag{S17}$$

Here n = 3, $^{c_i(t_j)}$ are the coefficients of each end-product to be optimized for the time delay selected, and $^{\Delta sM\,{}_{i}^{basis}(s)}$ is the fitting basis. $^{\sigma(s,t_j)}$ is the standard deviation of the experiment signal found by bootstrap analysis of $^{\Delta sM\,(s,t_j)}$ signal at the selected delay, for the theoretical signal fit, $^{\sigma(s,t_j)}$ is taken to be equal to 1. Using a multi-variable minimum search optimization routine, we get the optimized coefficients of end-products for the selected delay, which gives the best match to the signal by minimizing $^{Ft(c,\,t_j)}$ in the trusted region of 1.25 < s (Å^{-1}) < 7.5. This region in s for optimization is selected such that the artifacts found in the data are not considered in the fitting analysis. The optimized coefficients ($^{c_i(t_j)}$) are normalized by the sum of all optimized coefficients ($^{c_i(t_j)}$) to get the population estimate (yield) of each photoproduct for the pump-probe delay range selected. A similar method to determine the photoproducts population is described in detail in a prior reference[27].

The fitting analysis on the simulated data (convolved with experimental time-resolution), estimates the product yields to be 61.2 % cc-COD, 29.8 % ct-COD, and 9 % BCO. These results are comparable to the product yields predicted from the TSH simulation's end-product classification. The fit results along with the yields of the end-products in case of experimental data, are discussed in the main text. The fit results for the experiment signal averaged over time delays between 250 fs and 400 fs are: 87.4 $\pm$ _8.8 % cc-COD, 12.3 $\pm$ _7.1 % ct-COD, and 0.3 $\pm$ _1 % BCO. Figure S19 shows the comparison of the experiment signal with the fitted signal and the simulated signal scaled by the excitation percentage. There is a good match between these signals, the reduced chi-square value (χ^2) was found to be 1.73 and 1.69 for the fitted signal and simulated signal (scaled), respectively. When averaged over later time delays between 400 fs and 900 fs, the fit yields 87.7 $\pm$ 6.1 % cc-COD, 12.3 $\pm$ 4.9 % ct-COD, and 0.0 $\pm$ 0.0 % BCO. We observe from the experimental ΔsM signal (Figure S6) that the signal intensity for these later time delays remains similar compared to the signal at the early delays between 250 fs and 400 fs, which is reflected in the fit results.

Figure S20 shows the averaged ΔsM signal for cc-COD and ct-COD products including the products with hydrogen migration. We can see that the hot cc-COD and [1,5]-H-shift-cc-COD follow the same pattern, with small differences which are below the experimental determination, so we took an average of these signals to get the basis for the combined hot cc-COD product. [4,8]-H-shift-cc-COD has only one trajectory, it is predicted to be less that 1% of total products estimated, and therefore was not included in the fitting. We can see that the ct-COD, [1,5]-H-shift-ct-COD, and [4,8]H-shift-ct-COD have almost identical patterns, therefore we took an average of these signals to get the basis for the combined ct-COD product.

End-Products	cis,cis-1,3-cyclooctadiene **(cc-COD)**			cis,trans-1,3-cyclooctadiene **(ct-COD)**			**Bicyclo [4.2.0] oct-7-ene**
	Hot ccCOD	[1,5]-H-shift-ccCOD	[4,8]-H-shift-ccCOD	ctCOD	[1,5]-H-shift-ctCOD	[4,8]-H-shift-ctCOD	BCO
Number of Trajectories	64	8	1	20	10	7	6
	73			37			
% of Trajectories	55.1 %	6.9 %	0.9 %	17.2 %	8.6 %	6 %	5.2 %
	63%			32%			5%

Table S1: End-products classification and percentage estimated from simulations.

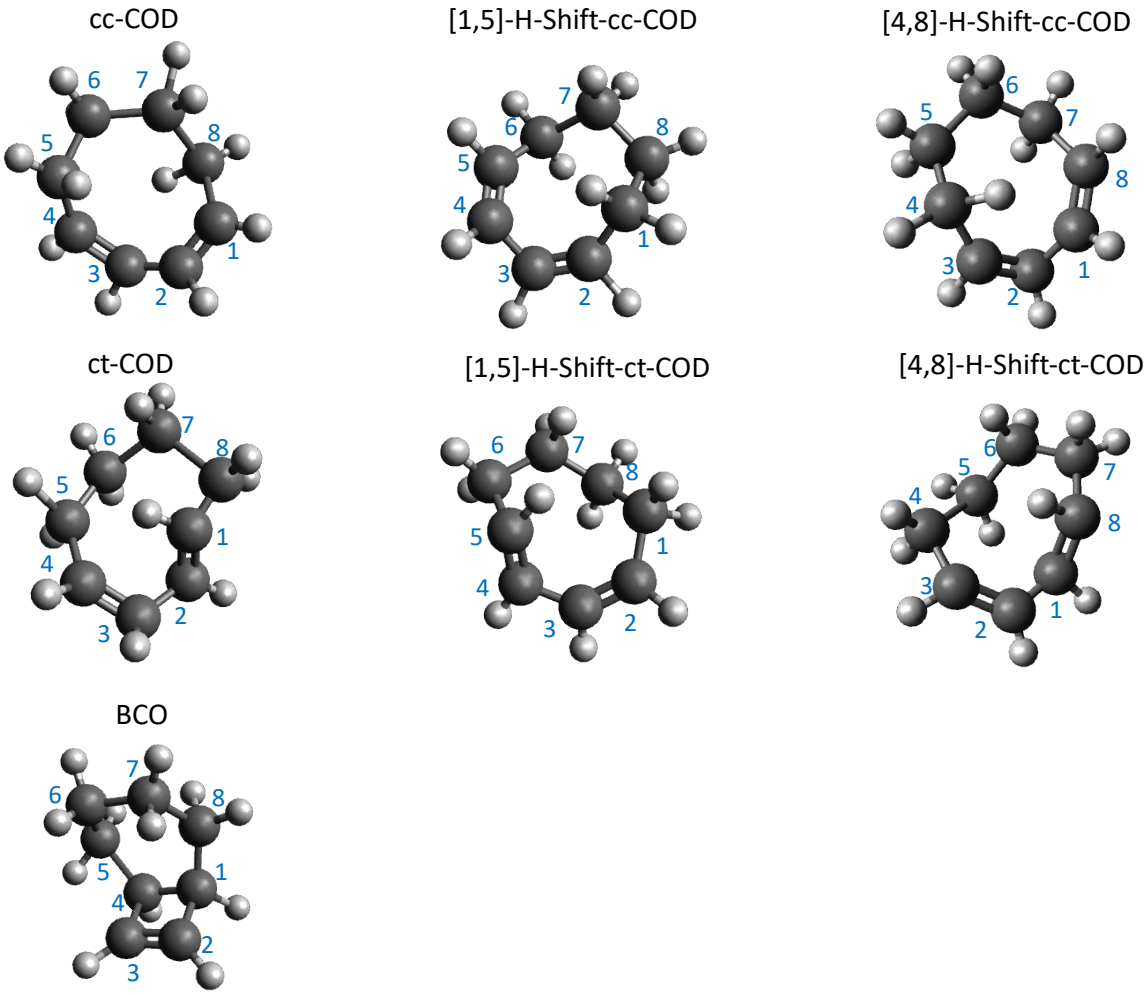

Figure S1: Representative structures of end-products formed. The figure shows each representative structure of the final photoproduct obtained from a trajectory forming that end-product, at a pump prob delay of 350 fs. The end-products formed include – hot cc-COD, ct-COD, BCO, [1,5]-H-shift-cc-COD, [1,5]-H-shift-ct-COD, [4,8]-H-shift-cc-COD, and [4,8]-H-shift-ct-COD. In the four end-products of H-shift, hydrogen migration takes place across the ring between C5 to C1 or C8 to C4, and these products behave either like cc-COD or ct-COD.

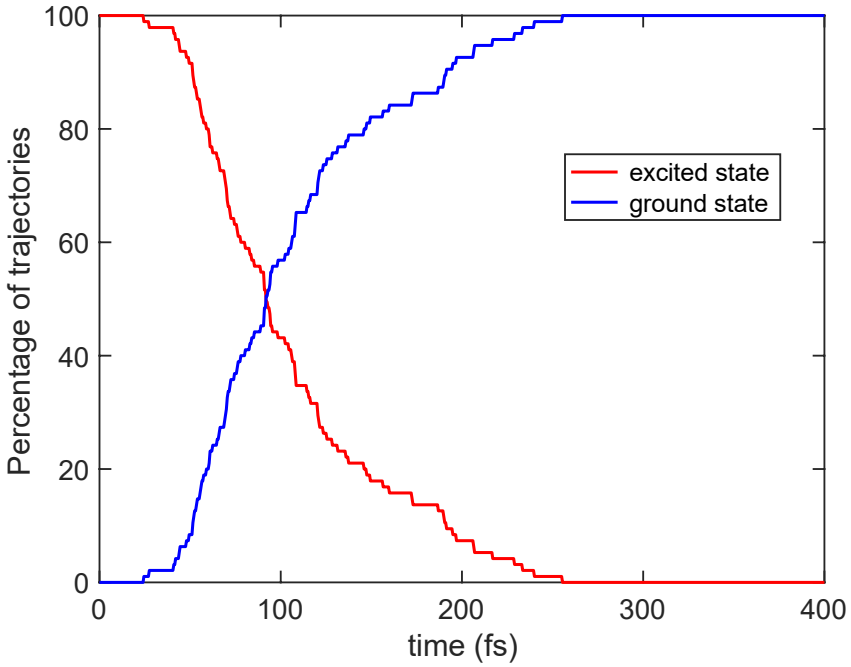

Figure S2: Population of trajectories in excited and ground state with respect to delay: The population of trajectories in the excited state and ground state is shown by red color and blue color line.

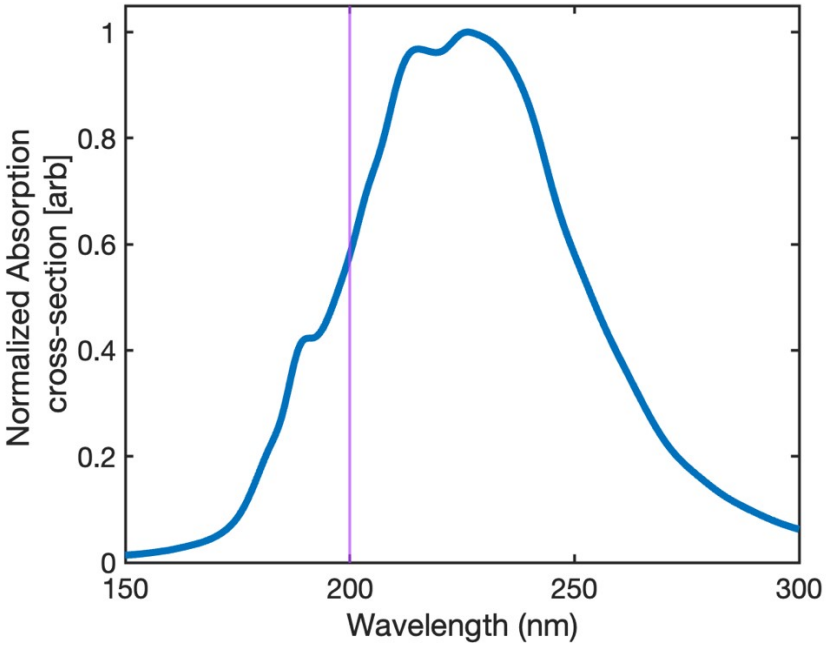

Figure S3: Normalized simulated absorption cross-section spectrum of cc-COD in the deep UV wavelengths range. The purple line corresponds to the excitation wavelength (200 nm or 6.2 eV) used in our experiment.

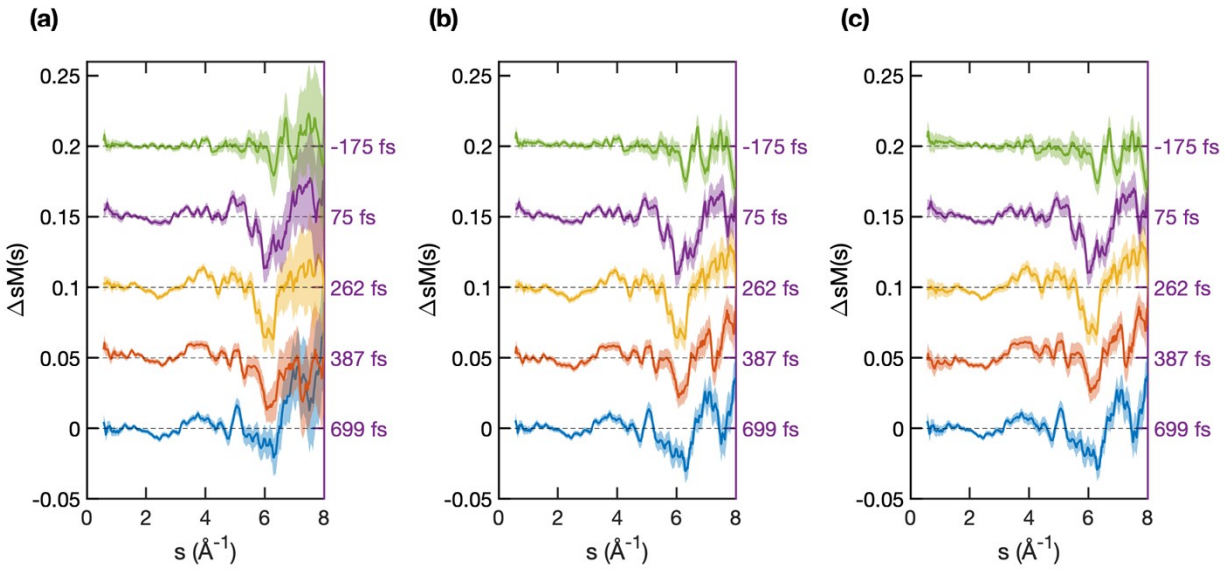

Figure S4: Delay dependent offset removal of the diffraction signal. (a), (b) and (c) shows the experiment difference-modified scattering intensity in momentum space (ΔsM) at different delays plotted for each delay before any additional background subtraction, after background subtraction with a low-order power fit, and after background subtraction using a combined low-order power and polynomial fits. Each delay is plotted with different color, and the delay information is labeled on the right side of y axis. The shaded region represents the error bars with one standard deviation from mean of the bootstrapped data.

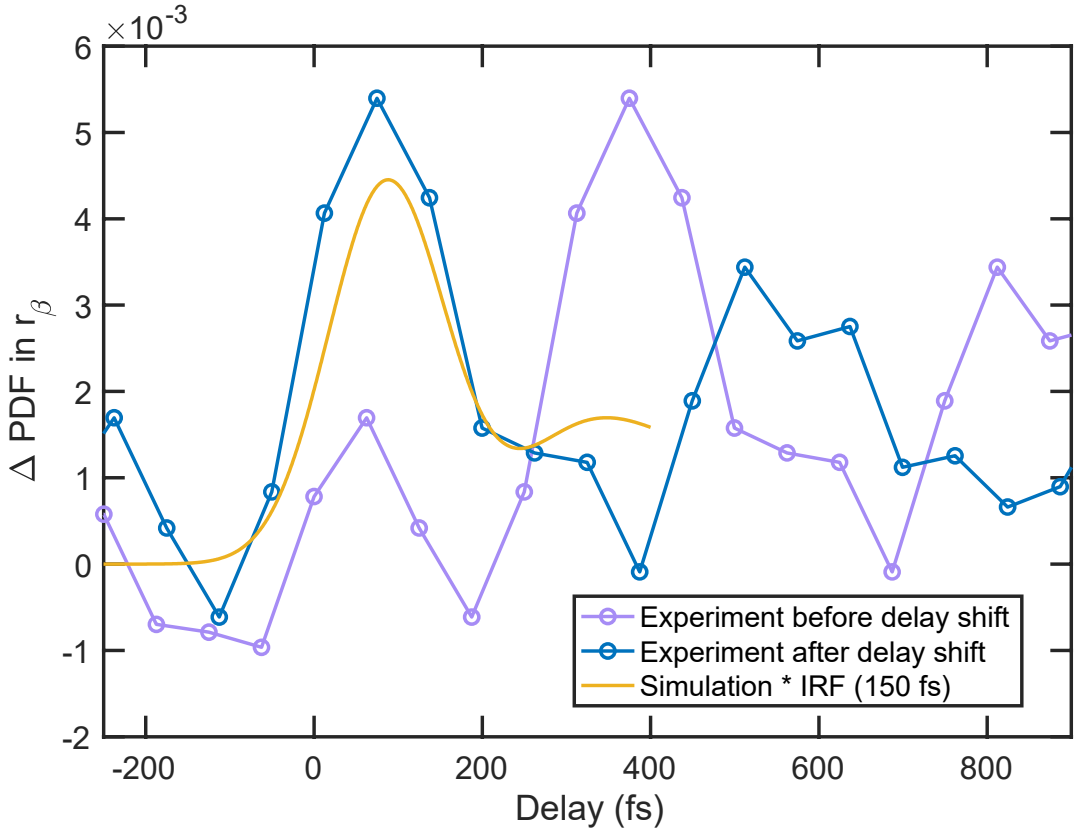

Figure S5: Experiment time zero determined from ΔPDF. The figure shows experiment before delay shift (purple line), experiment after delay shift (blue line), and simulated (yellow line) ΔPDF, respectively, averaged in $2.6 < r\ (\text{Å}) < 3$. The experiment data is shifted by 300 fs to qualitatively match the simulated data. The 300-fs shift in delays is with respect to the $\text{Delay}_{\text{solid}}$ (delay points determined by solid sample).

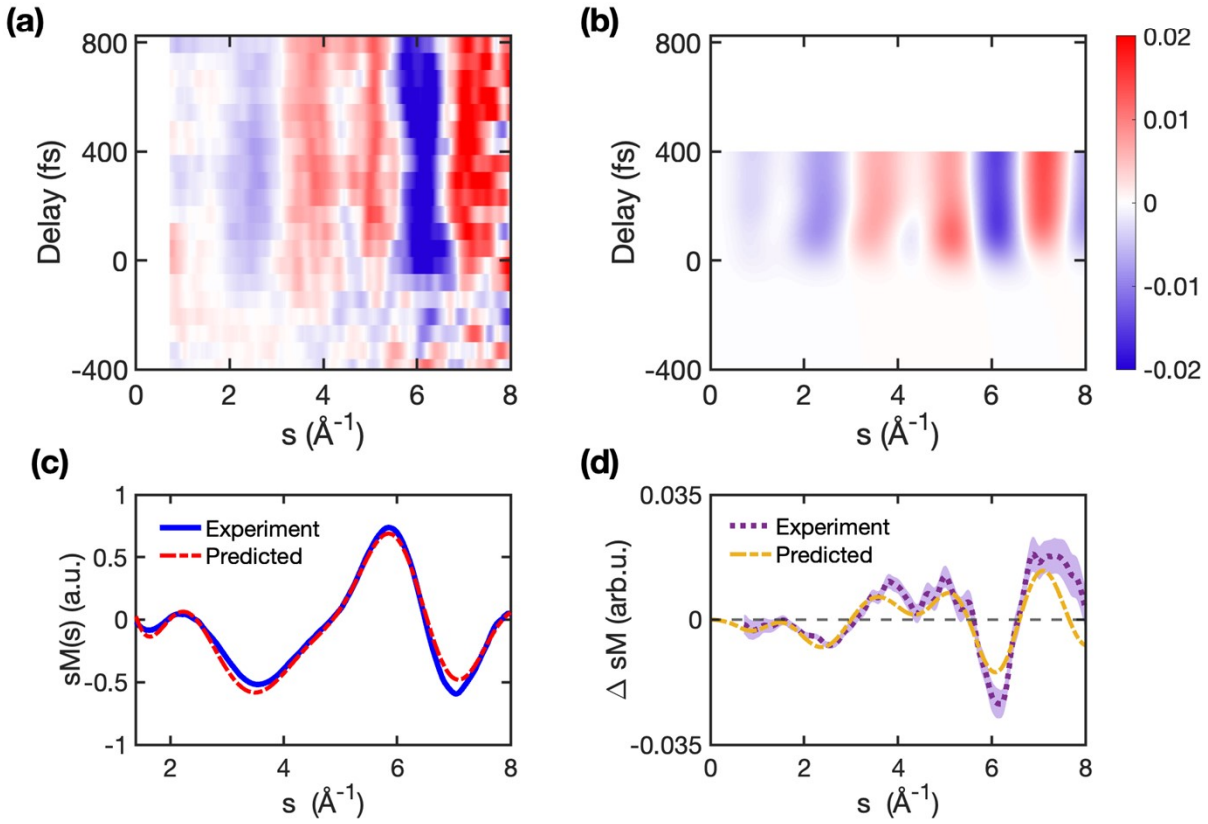

Figure S6: Experimental and simulated static sM and ΔsM: Panel (a) and (b) shows the difference diffraction signal (ΔsM (s, t)) in momentum space as the function of pump-probe delay for experiment, and simulation with time smoothing of 150 fs (IRF), respectively. Panel (c) shows the static sM(s) signal for experiment (blue) and simulation (broken red line) scaled (1.93 factor) to match experiment. Panel (d) shows the experimental (dotted purple line) and simulated (yellow line) ΔsM, respectively, averaged in 250 fs to 400 fs. The shaded area in Panels (d) represents the one-standard deviation error bars in the experiment signals calculated from the bootstrapping analysis. The simulated data is scaled with 0.0325 (excitation ratio), to match the experiment data.

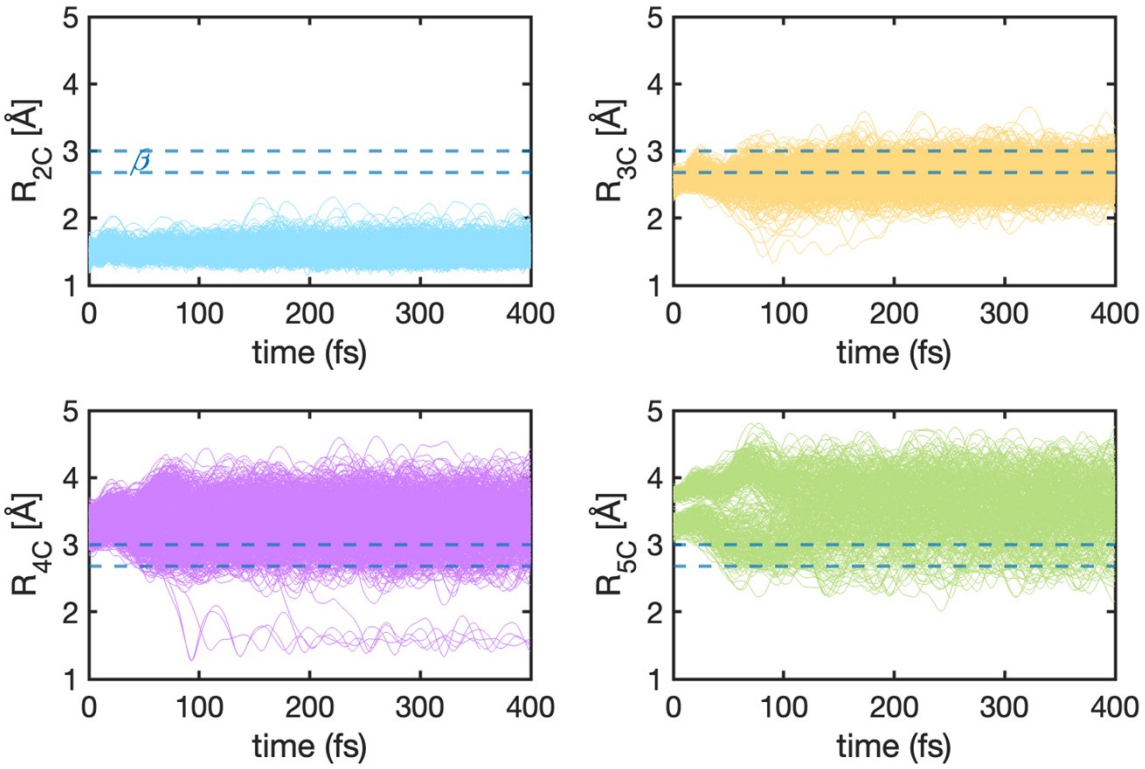

Figure S7: Changes in carbon distances of the molecule after excitation: The four panel shows the R_{2C}, R_{3C}, R_{4C} and R_{5C} carbon distances in blue, yellow, purple and green color lineouts. The region β ($2.6 < r(\text{Å}) < 3$) is marked in broken blue lines in all the panels.

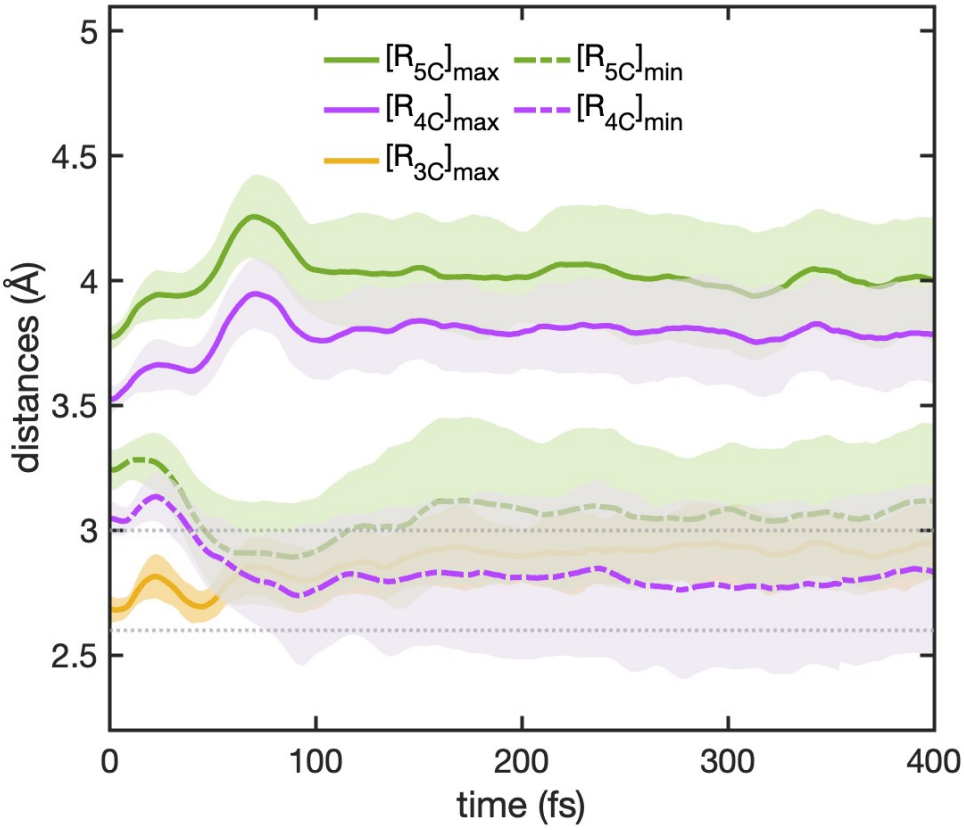

Figure S8: Tracking changes in largest and shortest unbonded carbon distances: The solid lines in the figure show the mean of largest R_{3C}, R_{4C} and R_{5C} carbon distances over all trajectories, in yellow, purple and green color. The broken lines in purple and green color show the mean of shortest R_{4C} and R_{5C} carbon distances over all trajectories. The shaded region around the lines represents the one-standard deviation across all the trajectories. The region β ($2.6 < r(\text{Å}) < 3$) is marked in dotted grey line.

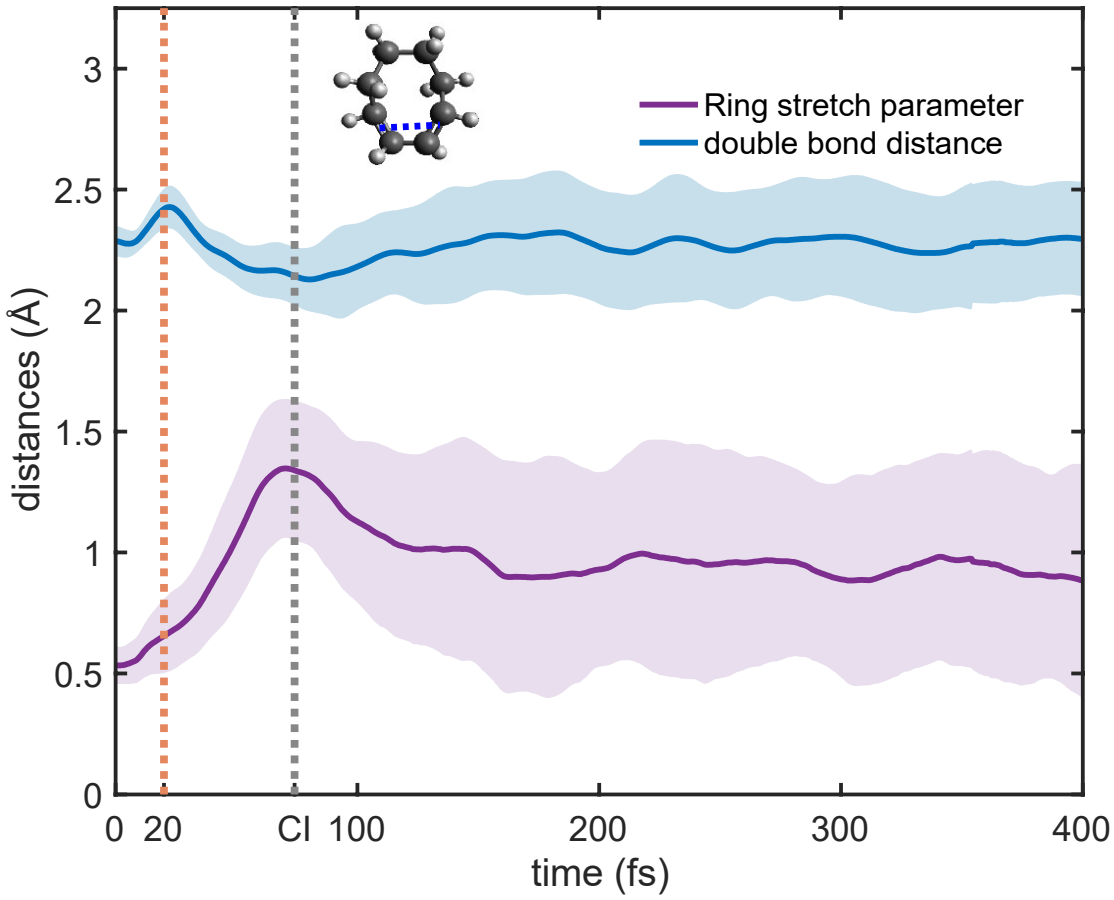

Figure S9: The double bonds distance changes after excitation. The distance between double bonds (from simulations) in the molecule for each delay is shown by the blue color lineout. The ring stretch parameter averaged over the simulated trajectories as a function of time-delay ($\varepsilon_{avg}(t)$) is shown by the purple color lineout. The shaded areas in both plots represents the one standard deviation over mean from the trajectories (95) simulated. The ring expands till delay equal to 20 fs (orange dotted line) and the most probable time for the wavepacket to reach conical intersection seam point is shown by grey dotted line. The inset shows the distance between double bonds marked in blue dotted line in the representative structure of cc-COD molecule at CI.

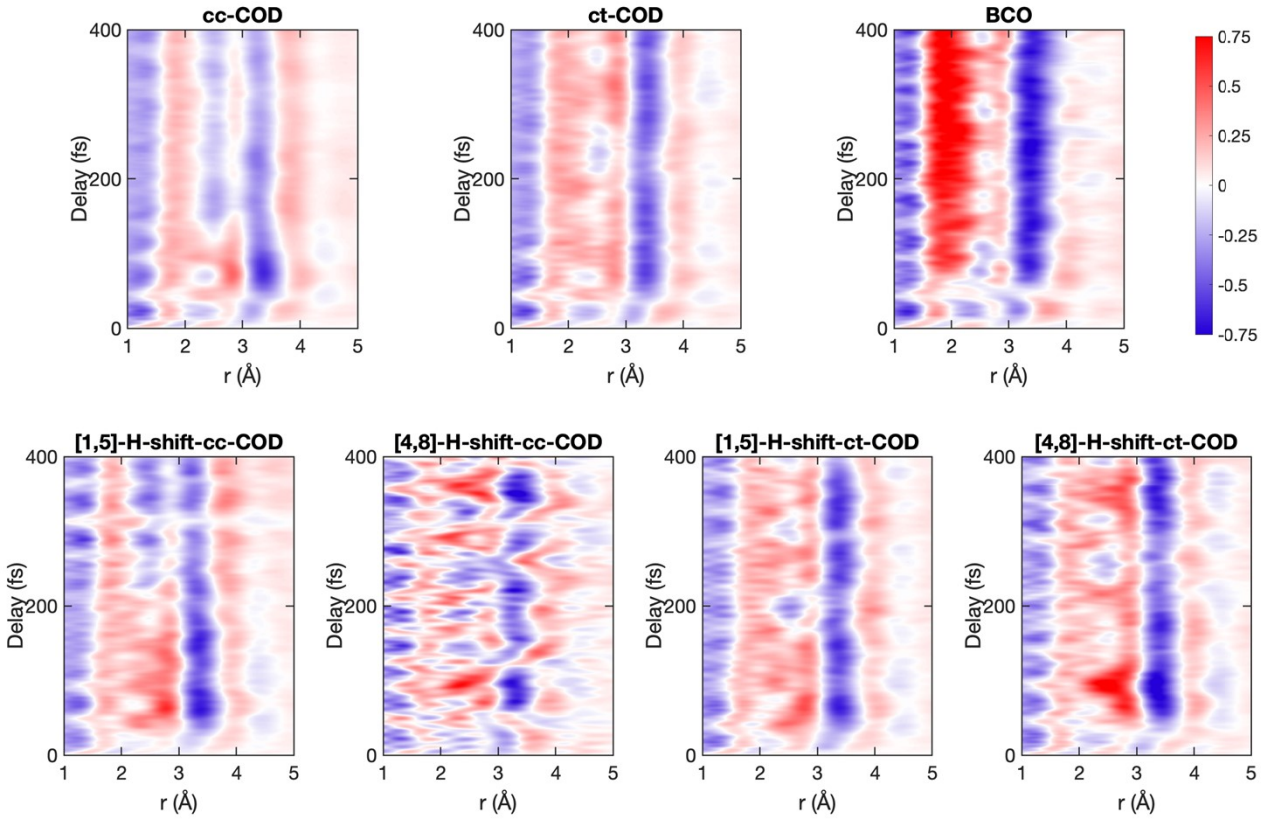

Figure S10: Time-dependent ΔPDF for all end-products. The seven panels show the ΔPDF signal of each end product predicted from simulation. The ΔPDF signal corresponding to each end-product is calculated by taking average of the combined signal from the trajectories forming that end-product.

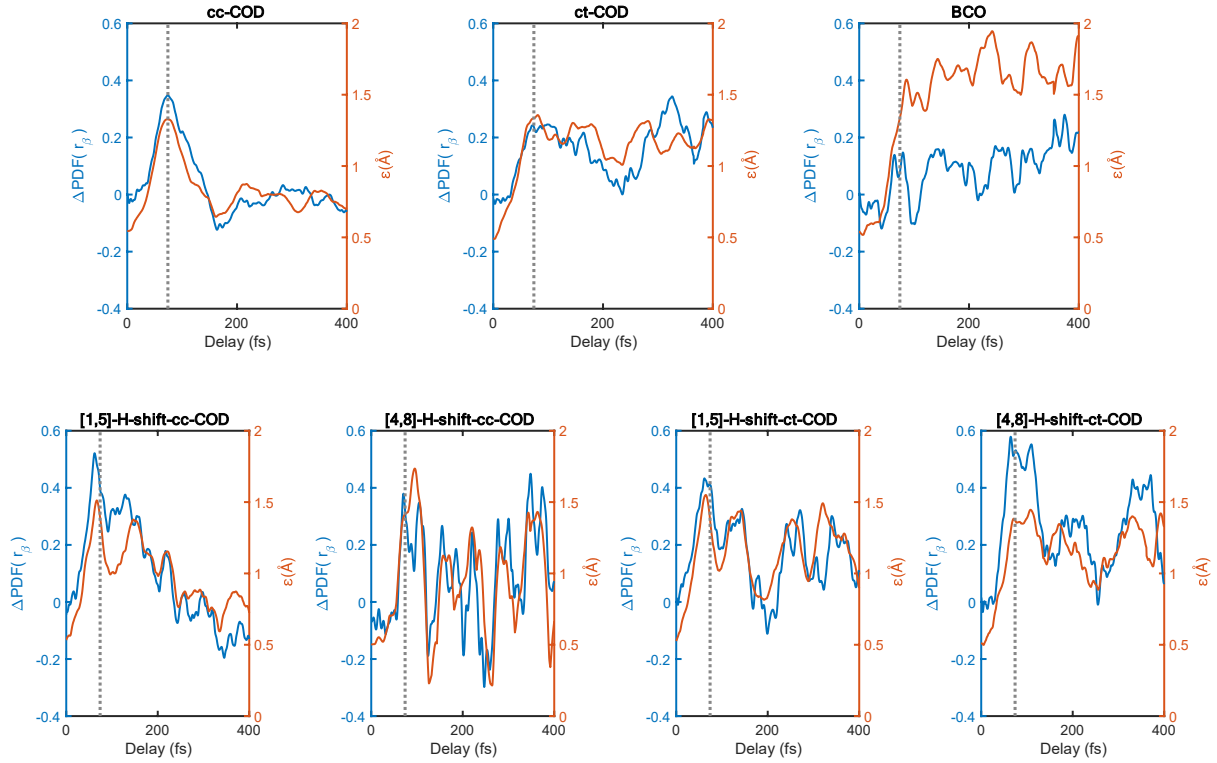

Figure S11: Oscillations in ΔPDF signal of all end-products due to ring stretching motion. Each panel shows the ΔPDF signal average in β ($2.6 < r(\text{Å}) < 3$) region is shown on the left y axis (blue color), and the ring stretch parameter average for the product (red) is shown on the right y axis, for each end-product. The most probable time for the wavepacket to reach the conical intersection seam point is shown by grey dotted line in all panels.

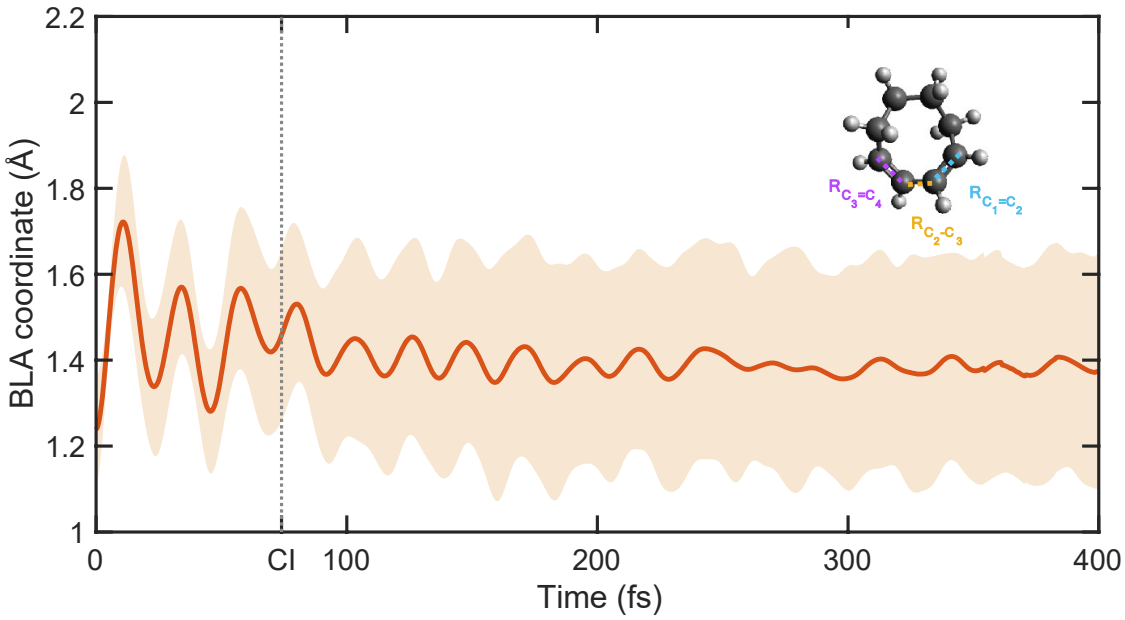

Figure S12: Bond length alternation (BLA) coordinate changes after excitation. The changes in the BLA coordinate averaged motion over all simulated trajectories is shown by the red color lineout. The shaded area represents the one standard deviation over mean from the trajectories (95) simulated. The most probable time for the wavepacket to reach the conical intersection seam point is shown by grey dotted line. The distances $R_{C_1=C_2}$, $R_{C_2-C_3}$, $R_{C_3=C_4}$ are labelled in the representative structure of cc-COD molecule in ground state, as shown in the inset.

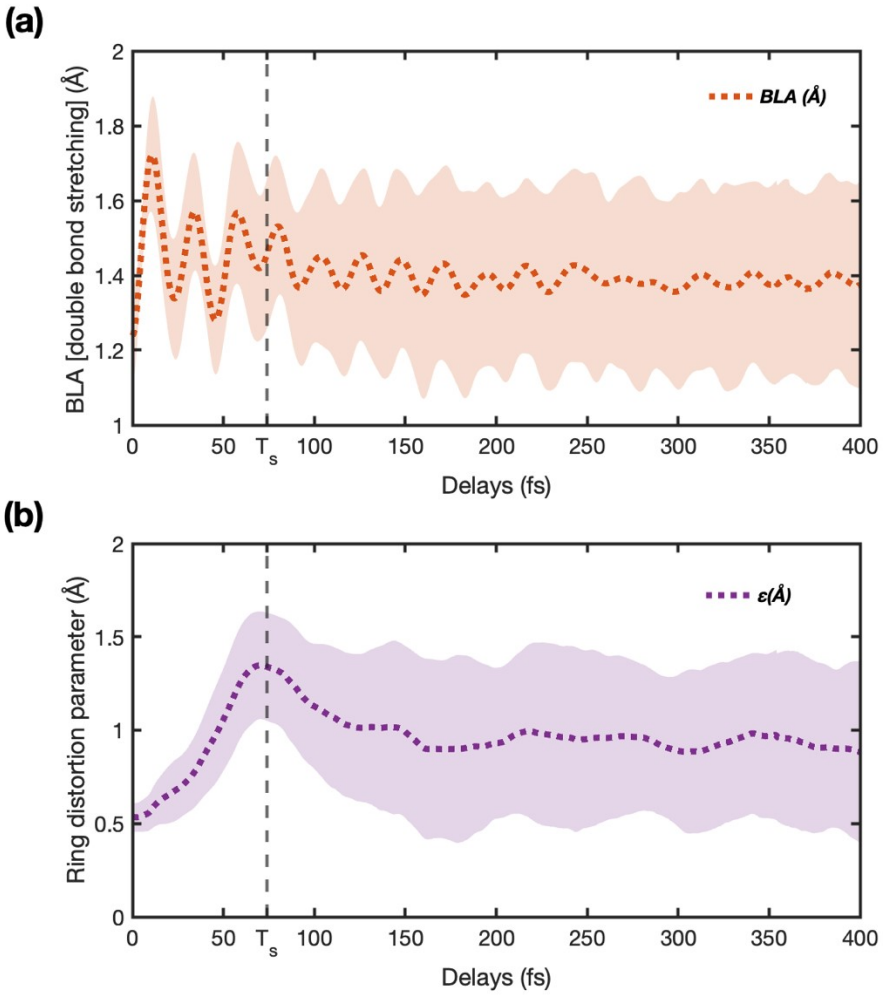

Figure S13: Comparison of ring distortion and bond length alternation (BLA) coordinate changes as a function of delay after excitation. The dotted lines in red in panel (a), and in purple in panel (b) show the evolution of the BLA, and ring distortion motions (ε(t)) parameters, respectively, averaged over all simulated trajectories (95). The shaded area represents the one standard deviation over mean from the trajectories simulated. The vertical grey broken line in all panels marks the most likely time (74 fs) for the wave packet to reach the CI seam.

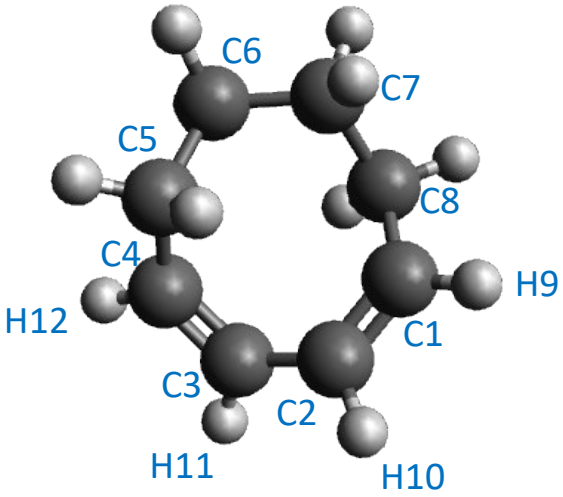

Figure S14: Cis-cis-1,3-cyclooctadiene (cc-COD) ground state molecule with carbon and hydrogen atoms labelled.

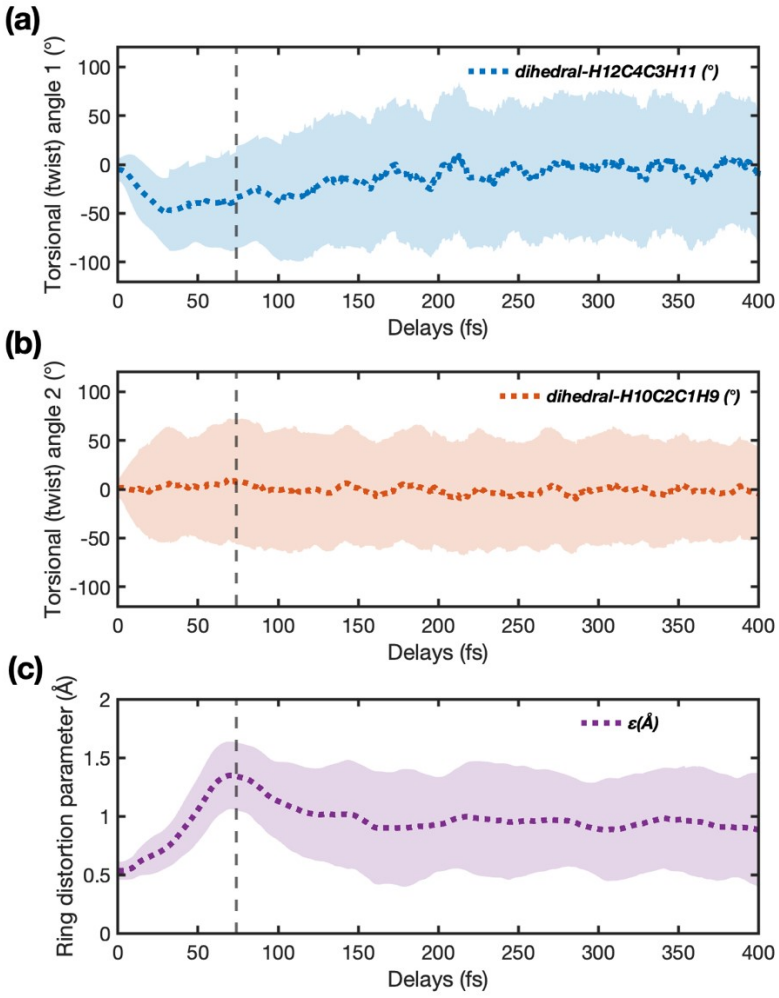

Figure S15: Comparison of torsional or twist angles of double bonds with ring distortion motion. The dotted lines in blue in (a), red in (b) and in purple in (c) shows the mean torsional angle 1, the mean torsional angle 2, and mean ring distortion parameter ($\varepsilon(t)$), respectively, over all the simulated trajectories (95). The shaded area shows the standard deviation across all trajectories. The vertical grey broken line in all panels marks the most likely time (74 fs) for the wave packet to reach the CI seam.

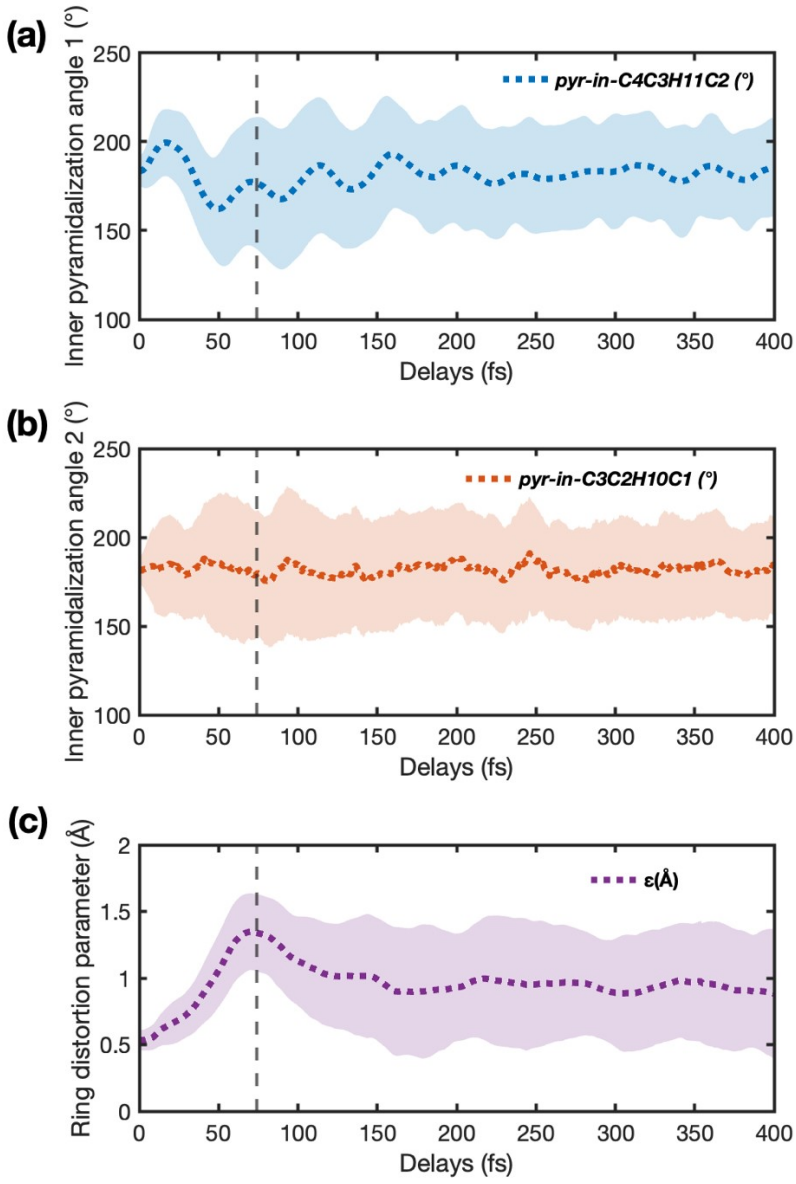

Figure S16: Comparison of inner pyramidalization angles of both double bonds with ring distortion motion. The dotted lines in blue in (a), red in (b) and in purple in (c) shows the mean inner pyramidalization angle 1, the mean inner pyramidalization angle 2, and mean ring distortion parameter (ε(t)), respectively, over all the simulated trajectories (95). The shaded area shows the standard deviation across all trajectories. The vertical grey broken line in all panels marks the most likely time (74 fs) for the wave packet to reach the CI seam.

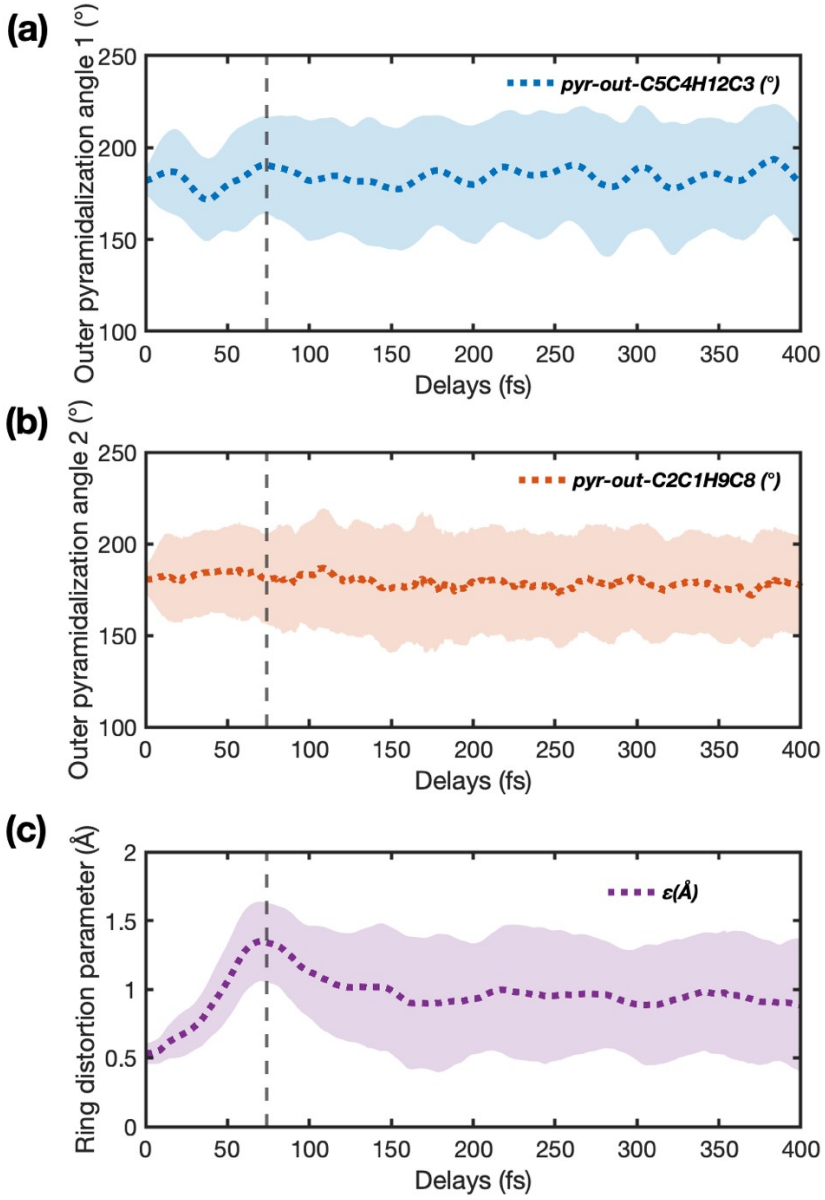

Figure S17: Comparison of outer pyramidalization angles of both double bonds with ring distortion motion. The dotted lines in blue in (a), red in (b) and in purple in (c) shows the mean outer pyramidalization angle 1, the mean outer pyramidalization angle 2, and mean ring distortion parameter (ε(t)), respectively, over all the simulated trajectories (95). The shaded area shows the standard deviation across all trajectories. The vertical grey broken line in all panels marks the most likely time (74 fs) for the wave packet to reach the CI seam.

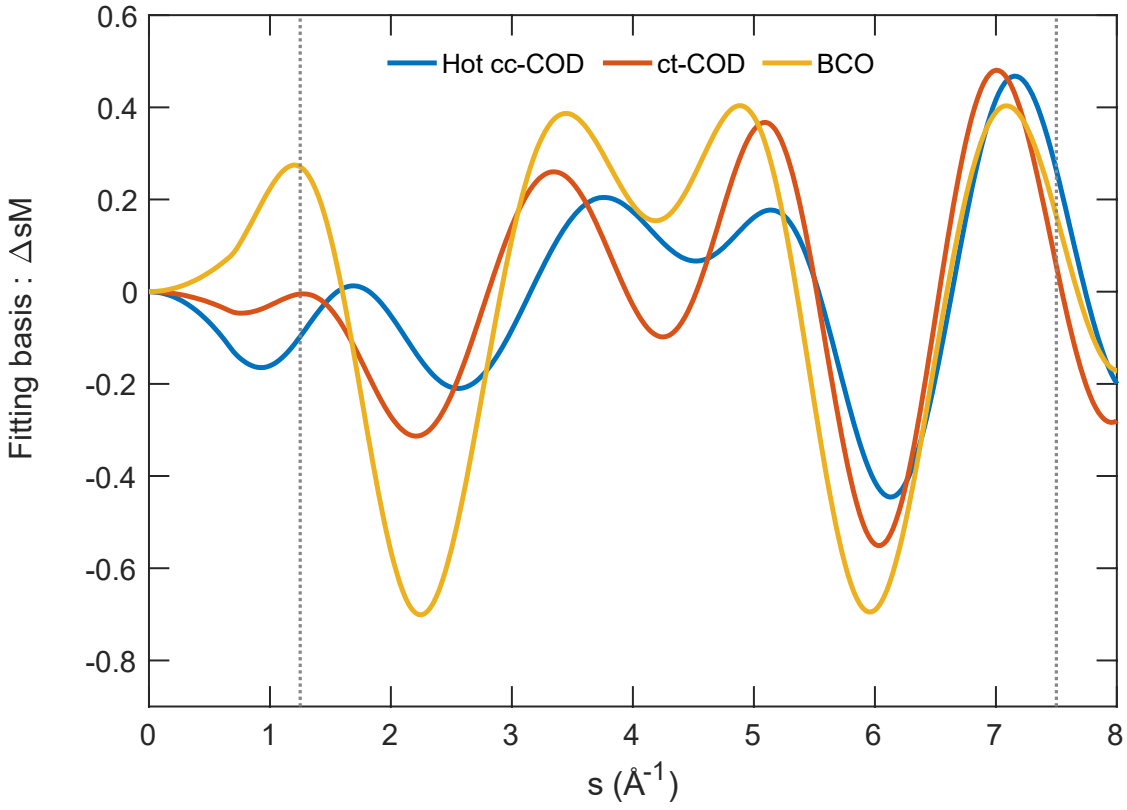

Figure S18: Fitting basis. The ΔsM signal average for delays 250 fs <t < 400 fs, for the combined hot cc-COD (blue), combined ct-COD (red) and BCO (yellow) products are shown. These signals are the basis for the fitting analysis performed. The region of trust, 1.25 < s (Å^{-1}) < 7.5, used for fitting analysis is marked in grey dotted lines.

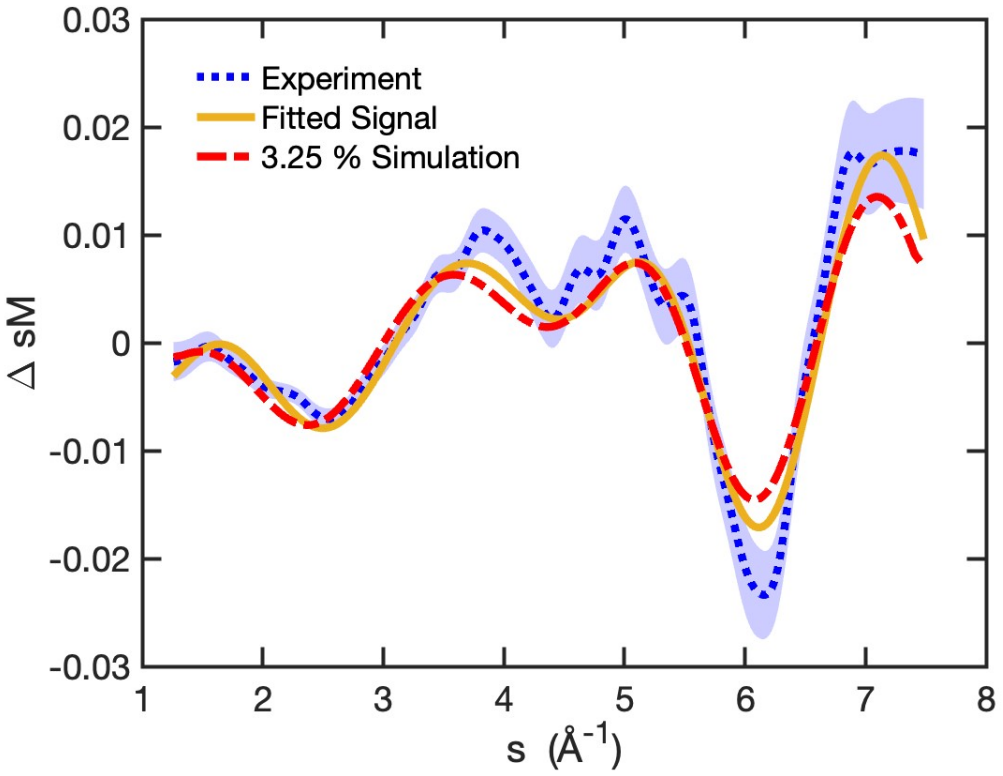

Figure S19: Comparison of experimental, fitted and simulated signal. ΔsM signal average for delays 250 fs <t < 400 fs for experimental (dotted blue line) and simulated signal scaled with excitation percentage of 3.25 % (broken red line) is shown. The shaded area represents the estimated error (one standard deviation) in experiment signal from the bootstrapped data. Yellow line represents the fitted signal to the experiment from the fitting analysis.

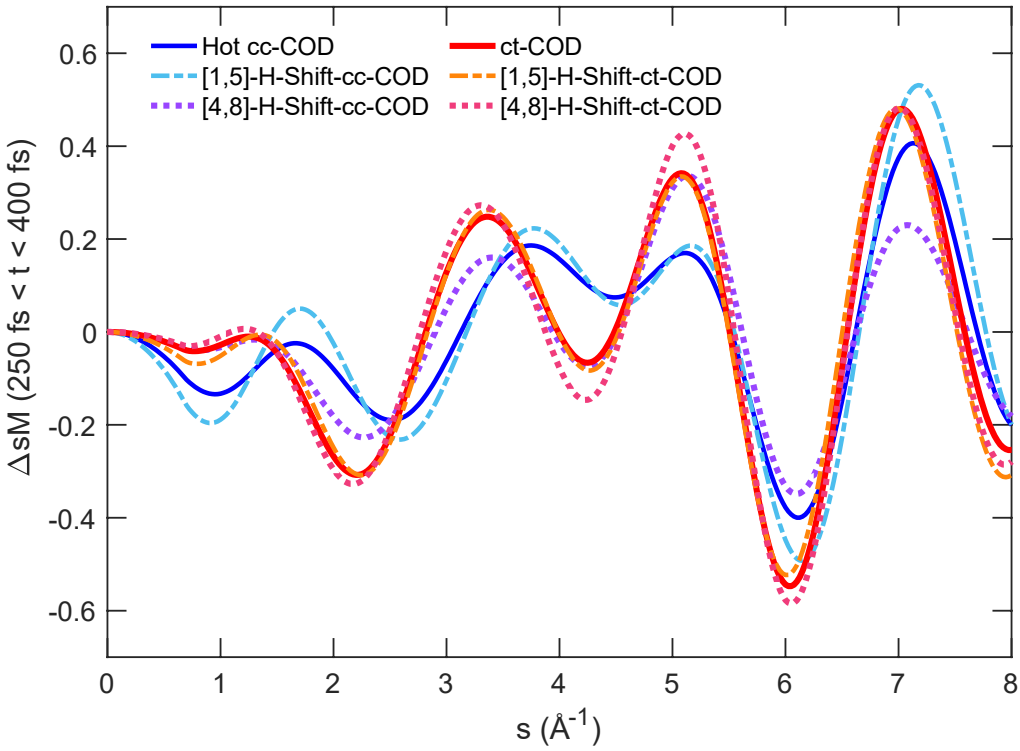

Figure S20: ΔsM signal for hot cc-COD, ct-COD and Hydrogen shifts products. The simulated ΔsM signal average for delays 250 fs <t < 400 fs of hot cc-COD (solid blue), [1,5]-H-shift-ccCOD (broken light blue), [4,8]-H-shift-ccCOD (dotted purple), ct-COD (solid red), [1,5]-H-shift-ct-COD (broken orange), and [4,8]-H-shift-ct-COD (dotted pink) is shown.

References

1 J. Yang, X. Zhu, J. P. F. Nunes, J. K. Yu, R. M. Parrish, T. J. A. Wolf, M. Centurion, M. Gühr, R. Li, Y. Liu, B. Moore, M. Niebuhr, S. Park, X. Shen, S. Weathersby, T. Weinacht, T. J. Martinez and X. Wang, *Science*, 2020, **368**, 885–889.

2 J. P. F. Nunes, M. Williams, J. Yang, T. J. A. Wolf, C. D. Rankine, R. Parrish, B. Moore, K. Wilkin, X. Shen, Ming-Fu Lin, K. Hegazy, R. Li, S. Weathersby, T. J. Martinez, X. J. Wang[i] and M. Centurion, *Phys. Chem. Chem. Phys.***,** 2024, **26**, 17991-17998.

3 T. J. A. Wolf, D. M. Sanchez, J. Yang, R. M. Parrish, J. P. F. Nunes, M. Centurion, R. Coffee, J. P. Cryan, M. Gühr, K. Hegazy, A. Kirrander, R. K. Li, J. Ruddock, X. Shen, T. Vecchione, S. P. Weathersby, P. M. Weber, K. Wilkin, H. Yong, Q. Zheng, X. J. Wang, M. P. Minitti and T. J. Martínez, *Nat. Chem.*, 2019, **11**, 504–509.

4 Y. Liu, D. M. Sanchez, M. R. Ware, E. G. Champenois, J. Yang, J. P. F. Nunes, A. Attar, M. Centurion, J. P. Cryan, R. Forbes, K. Hegazy, M. C. Hoffmann, F. Ji, M. F. Lin, D. Luo, S. K. Saha, X. Shen, X. J. Wang, T. J. Martínez and T. J. A. Wolf, *Nat Commun*, 2023, **14**, 2795.

5 J. Finley, P. Å. Malmqvist, B. O. Roos and L. Serrano-Andrés, *Chem. Phys. Lett.*, 1998, **288**, 299-306.

6 A. A. Granovsky, *J. Chem. Phys.*, 2011, **134**, 214113.

7 T. Shiozaki, W. Gyroffy, P. Celani and H. J. Werner, *J. Chem. Phys.*, 2011, **135**, 081106.

8 P. Chakraborty, Y. Liu, T. Weinacht and S. Matsika, *J. Chem. Phys.*, 2020, **152**, 174302.

9 Y. Liu, P. Chakraborty, S. Matsika and T. Weinacht, *J. Chem. Phys.*, 2020, **153**, 074301.

10 B. O. Roos, P. R. Taylor and P. E. Sigbahn, *Chem. Phys.*, 1980, **48**, 157-173.

11 T. H. Dunning, *J. Chem. Phys.*, 1989, **90**, 1007–1023.

12 M. Barbatti, M. Ruckenbauer, F. Plasser, J. Pittner, G. Granucci, M. Persico and H. Lischka, *Wiley Interdiscip. Rev.: Comput. Mol. Sci.*, 2014, **4**, 26–33.

13 Barbatti, M.; Granucci, G.; Ruckenbauer, M.; Plasser, F.; Crespo-Otero, R.; Pittner, J.; Persico, M.; Lischka, H. NEWTON-X: A package for Newtonian dynamics close to the crossing seam, version 2, 2016, http://www.newtonx.org.

14 T. Shiozaki, *Wiley Interdiscip. Rev.: Comput. Mol. Sci.*, 2018, **8**, e1331.

15 BAGEL, Brilliantly Advanced General Electronic-structure Library. http://www.nubakery.org under the GNU General Public License, (2017).

16 J. C. Tully, *J. Chem. Phys.,* 1990, **93**, 1061–1071.

17 G. Granucci and M. Persico, *J. Chem. Phys.*, 2007, **126**, 134114.

18 C. Zhu, S. Nangia, A. W. Jasper and D. G. Truhlar, *J. Chem. Phys.*, 2004, **121**, 7658–7670.

19 J. Towns, T. Cockerill, M. Dahan, I. Foster, K. Gaither, A. Grimshaw, V. Hazlewood, S. Lathrop, D. Lifka, G. D. Peterson and R. Roskies, *Comput. Sci. Eng.*, 2014, **16**, 62-74.

20 C. Cisneros, Master Thesis, California State University, Long Beach, 2022.

21 F. Salvat, A. Jablonski and C. J. Powell, *Comput. Phys. Commun.*, 2005, **165**, 157-190.

22 H. Ihee, B. M. Goodson, R. Srinivasan, V. A. Lobastov and A. H. Zewail, *J. Phys. Chem. A*, 2002, **106**, 4087–4103.

23 H. Ihee, V. A. Lobastov, U. M. Gomez, B. M. Goodson, R. Srinivasan, C. Y. Ruan and Zewail, A.H., *Science,* 2001, **291**,458-462.

24 H. Ihee, J. Cao and A. H. Zewail, *Chem. Phys. Lett.*, 1997, **281**, 10–19.

25 S. P. Weathersby, G. Brown, M. Centurion, T. F. Chase, R. Coffee, J. Corbett, J. P. Eichner, J. C. Frisch, A. R. Fry, M. Gühr, N. Hartmann, C. Hast, R. Hettel, R. K. Jobe, E. N. Jongewaard, J. R. Lewandowski, R. K. Li, A. M. Lindenberg, I. Makasyuk, J. E. May, D. McCormick, M. N. Nguyen, A. H. Reid, X. Shen, K. Sokolowski-Tinten, T. Vecchione, S. L. Vetter, J. Wu, J. Yang, H. A. Dürr and X. J. Wang, *Rev. Sci. Instrum.*, 2015, **86**, 073702.

26 X. Shen, J. P. F. Nunes, J. Yang, R. K. Jobe, R. K. Li, M. F. Lin, B. Moore, M. Niebuhr, S. P. Weathersby, T. J. A. Wolf, C. Yoneda, M. Guehr, M. Centurion and X. J. Wang, *Struct. Dyn.*, 2019, **6**, 054305.

27 J. P. Figueira Nunes, L. M. Ibele, S. Pathak, A. R. Attar, S. Bhattacharyya, R. Boll, K. Borne, M. Centurion, B. Erk, M. F. Lin, R. J. G. Forbes, N. Goff, C. S. Hansen, M. Hoffmann, D. M. P. Holland, R. A. Ingle, D. Luo, S. B. Muvva, A. H. Reid, A. Rouzée, A. Rudenko, S. K. Saha, X. Shen, A. S. Venkatachalam, X. Wang, M. R. Ware, S. P. Weathersby, K. Wilkin, T. J. A. Wolf, Y. Xiong, J. Yang, M. N. R. Ashfold, D. Rolles and B. F. E. Curchod, *J. Am. Chem. Soc.*, 2024, **146**, 4134–4143.